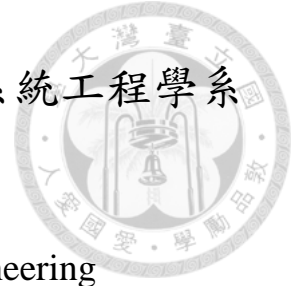


國立臺灣大學生物資源暨農學院生物環境系統工程學系



博士論文

Department of Bioenvironmental Systems Engineering

College of Bioresources and Agriculture

National Taiwan University

Doctoral Dissertation

變質量平滑粒子動力法在降雨逕流系統之模擬

Modeling rainfall-runoff processes using smoothed  
particle hydrodynamics with mass-varied particles

張佑聖

Yu-Sheng Chang

指導教授：張倉榮 博士

Advisor : Tsang-Jung Chang, Ph.D

中華民國 106 年 5 月

May, 2017



國立臺灣大學博士學位論文  
口試委員會審定書

變質量平滑粒子動力法在降雨逕流系統之模擬

Modeling Rainfall-Runoff Processes Using Smoothed Particle  
Hydrodynamics with Mass-Varied Particles

本論文係張佑聖君（學號 D01622002）在國立臺灣大學生物環境系統工程學系(所)完成之博士學位論文，於民國 106 年 5 月 27 日承下列考試委員審查通過及口試及格，特此證明

口試委員：

張佑聖

(簽名)

葉真豪 (指導教授)

許銘熙

柳文成

陳明志

張佑聖

系主任、所長

林銘材

(簽名)



## 謝 誌



本論文之順利完成，最要感謝始終給予我細心指導與諄諄教誨的恩師 張倉榮教授。感謝老師張倉榮教授長久以來對我的照顧與包容，在我論文的撰寫上以及研究的學習上，不厭其煩地給我教導，對我在研究態度與人生旅途上獲益良多。博士論文口試期間，承蒙口試委員許銘熙教授、陳明志教授、柳文成教授及葉克家教授提供良多的意見與建議，使得本論文內容更加充實及嚴謹，謹此向諸位教授致上萬分謝意。

感謝宏名學長、藜穎學姊、高華學長、嘉和學長、俊龍學長、祥麟等生物環境力學研究室畢業的學長姐們、同伴、同學與學弟妹給予許多重要的支援，還有許多高中、大學、研究所及不同時期的好朋友們，謝謝你們陪我一同走過這一段路。也謝謝那些曾經幫助過我的每一位師長及人生旅途中的過客。

最後，感謝我的父母及家人，總是默默地在背後支持著我，讓我能夠毫無後顧之憂地專注在學業上。

畫下這段旅途的一個句點，新的挑戰及更廣大的世界才剛要開始等著我去面對及發掘！



## 摘要

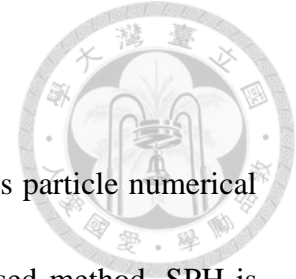
平滑粒子動力法(Smoothed Particle Hydrodynamics, SPH)為一種拉格朗日(Lagrange)觀點下的無網格粒子數值模擬方法。相較於傳統固定式網格數值方法, SPH 在處理自由液面與大形變流場問題上已被許多研究證實具有優勢。近期 SPH 被運用在求解淺水波方程式(shallow water equations, SWEs)去模擬或是處理各種水力學問題, 而發展出 SPH-SWEs 模式。然而, 由於 SWEs 維度上的限制, 目前 SPH-SWEs 無法處理計算維度外流體增減的問題, 如側流、降雨和入滲等現象。因此本研究發展變質量平滑粒子動力法, 藉由流體粒子質量的增加或減少來模擬額外維度上流體的增減, 並將此新模式運用於研究降雨逕流過程中相關之問題上。

為了測試此新發展之變質量 SPH 法, 研究中選取了三個具有代表性的案例進行模擬。模擬案例包含一維平坦傾斜渠道上的均勻降雨、一維三坡度渠道上不同降雨延時之非均勻降雨與二維複雜地形上之均勻降雨。模擬結果顯示本研究所發展之模式可以不使用源項函數以及增加粒子數來處理增加的流體質量, 且在降雨經流過程中所出現的水躍、乾溼床移動邊界流及超臨界/亞臨界/跨流等現象上, 皆有不錯的吻合程度, 因而證明了此變質量 SPH 法的穩健與可靠性。

本研究中亦將此變質量 SPH 法在運用於處理入滲的問題上, 結合霍頓(Horton)入滲方程進行求解, 模擬逕流時流體減少之現象。另外, 本研究亦嘗試以兩分量壓力近似法(Two-component Pressure Approach, TPA)建立一維 SPH 下水道模式。藉由 TPA 可使得 SPH 能以單一控制方程式來同時模擬滿管壓力流與自由液面流的流況。而透過變質量流體粒子的運用, 可將降雨逕流模式(增質量)、入滲模式(減質量)與下水道模式(質量傳輸)結合成一套 SPH 淹水模式。

**關鍵字：**平滑粒子動力法, 淺水波方程式, 無網格方法, 變質量粒子, 降雨逕流過程, 入滲, 下水道

## Abstract



Smoothed Particle Hydrodynamics (SPH) is a kind of meshless particle numerical method with Lagrangian concept. Compared to traditional grid-based method, SPH is proved by many researches that it has advantages on dealing with free surface and large deformation problems. Recently SPH has been implemented on solving shallow water equations (SWEs) for simulating or handling the hydrodynamic problems and SPH-SWEs has been developed accordingly. However, due to the limitation of dimensions of SWEs, SPH-SWEs still cannot process the problems of fluid inflow/outflow beyond the computational domain, e.g. lateral flow, rainfall, and infiltration, etc. Thus this research constructs the mass-varied SPH model which uses the mass variation of fluid particle to simulate the fluid inflow/outflow on the external dimension and also applies this new model on investigating the rainfall-runoff processes.

To validate this novel mass-varied SPH model, three benchmark case studies are adopted to conduct numerical simulations, including uniform rainfall over a 1D flat sloping channel, nonuniform rain falling over a 1D three-slope channel with different rainfall durations, and uniform rainfall over a 2D plot with complex topography. The simulated results indicate that the proposed treatment can avoid the necessity of a source term function of mass variation, and no additional particles are needed for the increase of mass. Rainfall-runoff processes can be well captured in the presence of

hydraulic jumps, dry/wet bed flows, and supercritical/subcritical/transcritical flows. The proposed treatment using mass-varied particles was proven robust and reliable for modeling rainfall-runoff processes.



In this thesis the mass-varied SPH model is also utilized on solving the infiltration problems associated with Horton formula to simulate the fluid decrease during the runoff process. In addition, this research tries to develop a one-dimensional SPH sewer model with two-component pressure approach (TPA). With this approach, SPH can simulate the full-pipe pressure flows and free surface flows at the same time with single governing equation. Afterwards in future study, by means of mass-varied fluid particles, we can integrate the rainfall-runoff model (mass addition), infiltration model (mass reduction) and sewer model (mass transfer) into a SPH flood model.

**Key words: Smoothed particle hydrodynamics, Shallow water equations, Meshless method, mass-varied particle, Rainfall-runoff process, Infiltration, Sewer.**





## Table of Contents

摘要.....	I
Abstract.....	II
Table of Contents.....	IV
List of Figures.....	VI
List of Tables.....	VIII
<b>Chapter 1 Introduction.....</b>	<b>1</b>
1.1 Objectives.....	1
1.2 Research method and SPH.....	2
1.3 Synthesis.....	6
<b>Chapter 2 Literature review.....</b>	<b>7</b>
2.1 SPH theory.....	7
2.1.1 Wall boundary condition.....	7
2.1.2 Inflow and outflow boundary.....	8
2.1.3 SPH formula modification.....	9
2.1.4 Particle searching.....	9
2.1.5 Error analysis.....	10
2.2 SPH application on shallow water equations and SPH-SWEs model.....	10
2.3 Rainfall-runoff processes and models.....	11
2.4 Infiltration.....	12
2.5 Drainage systems and sewers.....	13
<b>Chapter 3 Theories and Methods.....</b>	<b>16</b>
3.1 Introduction of SPH.....	16
3.2 Central concept and fundamental formulations.....	16
3.3 Particle approximation.....	18
3.4 Derivation of fundamental formulations.....	19
3.4.1 First derivative.....	20
3.4.2 Second derivative.....	21
3.5 The choices of kernel functions.....	22
<b>Chapter 4 SPH for shallow water equations and numerical techniques.....</b>	<b>25</b>
4.1 Shallow water equations and SPH-SWEs.....	25
4.2 Water depth/cross-section wetted area evolution.....	28
4.3 Using mass-varied particles and the modified smoothing length updating formulation.....	31
4.4 Discretization of the momentum equation.....	36

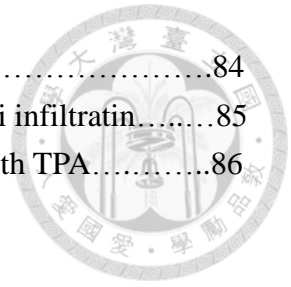
4.5 Evolution of bed gradient term and friction term.....	37
4.6 Velocity correction in momentum equation for mass variation and extreme small water depth.....	39
4.7 Artificial viscosity and stabilization term.....	40
4.8 Time stepping and integration.....	41
4.9 Nearest neighboring particle searching (NNPS).....	42
4.9.1 All-pair search.....	43
4.9.2 Linked-list.....	43
4.10 Wall boundary conditions.....	44
4.10.1 The Ghost particles method.....	45
4.10.2 The simplified MVBP method.....	46
4.10.3 Periodic boundary condition.....	49
4.11 Open boundary conditions.....	49
4.11.1 Method of specified time interval for 1D Q-A form of SWEs.....	50
4.11.2 Riemann invariants for 2D $u$ - $d_w$ form of SWEs.....	51
4.12 Green-Ampt Infiltration module.....	53
4.13 1D SPH sewer module.....	55
4.14 Calculation process.....	58
<b>Chapter 5 Model validations and applications.....</b>	<b>66</b>
5.1 Uniform rainfall over a 1D flat channel.....	67
5.1.1 Convergence analysis of the particle number.....	67
5.1.2 Numerical accuracies of discharge, water depth, velocity and Froude number.....	68
5.2 Nonuniform rainfall over a 1D three-slope channel.....	69
5.3 Uniform rainfall over a 2D plot with complex topography.....	70
5.3.1 Convergence analysis of the particle number.....	71
5.3.2 Numerical accuracies of discharge, water depth, velocity and Froude number.....	72
5.4 Green-Ampt infiltration.....	73
5.5 1D pipe flow with SPH-SWEs.....	74
<b>Chapter 6 Conclusions.....</b>	<b>87</b>
<b>References.....</b>	<b>89</b>



## List of Figures

<b>Figure 3.1</b> Particle approximation (Liu and Liu, 2003).....	24
<b>Figure 4.1</b> Definition sketch of SPH with shallow water equations.....	59
<b>Figure 4.2</b> (a) Hydrologic phenomena of rainfall, overland flows and river flows and (b) SPH-SWE modeling of hydraulic phenomena.....	60
<b>Figure 4.3</b> Variations in the smoothing length of a fluid particle with different water depths, (a) the smoothing length $h$ and water depth $d_w$ , (b) a smoothing length of $0.5 h$ and a water depth of $2d_w$ and (c) a smoothing length of $0.5$ $h$ , water depth of $d_w$ and additional water depth $\Delta d_w$ caused by rainfall.....	61
<b>Figure 4.4</b> Linked-list and neighbor particles (SPHysics).....	62
<b>Figure 4.5</b> Sweeping through grid cells in 2D domain (SPHysics).....	62
<b>Figure 4.6</b> Illustration of the ghost particles method.....	63
<b>Figure 4.7</b> Illustration of the MVB method illustration (Vacondio <i>et al.</i> , 2012b).....	63
<b>Figure 4.8</b> Illustration of periodic boundary: lateral periodic boundaries (SPHysics)....	64
<b>Figure 4.9</b> Sketch of the method of specified time interval (Chang and Chang, 2013) .....	64
<b>Figure 4.10</b> Illustration of pen boundary illustration: inflow zone and outflow zero....	65
<b>Figure 4.11</b> The calculation flow chart (Liu and Liu, 2003).....	65
<b>Figure 5.1</b> The simulated and measured hydrographs of the case study in section 5.1.....	77
<b>Figure 5.2</b> The simulated profiles of (a) water depth, (b) velocity and (c) Froude number along the channel at $t = 10$ s, 60 s and 160 s in case study in section 5.1.....	78
<b>Figure 5.3</b> The profile of bed elevation of the case study in section 5.2.....	79
<b>Figure 5.4</b> The simulated hydrography and the simulated profiles of water depth in the case study in section 5.2, (a) and (d) rainfall duration = 10 s, (b) and (e) rainfall duration = 20 s and (c) and (f) rainfall duration = 30 s.....	80
<b>Figure 5.5</b> The temporal evolution of the Froude number at the outlet of the second case study, (a) a rainfall duration = 10 s, (b) rainfall duration = 20 s and (c) rainfall duration = 30 s.....	81
<b>Figure 5.6</b> The topography of the 2D plot of the case study in section 5.3.....	82
<b>Figure 5.7</b> The correlation between the simulated and measured velocities at the 62 measured points of the case study in section 5.3.....	83
<b>Figure 5.8</b> The simulated contours of water depth, velocity and Froude number of the	

case study in section 5.3.....	84
<b>Figure 5.9</b> The simulated discharge by SPH-SWEs with Green-Apmi infiltratin.....	85
<b>Figure 5.10</b> The simulated result of SPH-SWEs for 1D pipe flow with TPA.....	86





## List of Tables

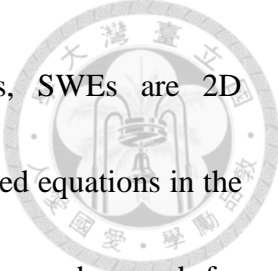
<b>Table 5.1</b> The $L_2$ norm errors based on the velocity at $t = 60$ s for four different particle numbers in the first case study.....	76
<b>Table 5.2</b> The $L_2$ norm errors based on the velocity for four different particle numbers in the third case study.....	76



## Chapter 1 Introduction

### 1.1 Objectives


The objective of this thesis is to implement Smoothed Particle Hydrodynamics (SPH) on investigation and application of river hydraulics and ground overland flows and to develop an effective and robust numerical method. SPH is a Lagrangian meshless numerical method which discretizes the physical domain with moving particles. Without the restriction of grids, SPH has remarkable performance on large deformation problems especially for flow conditions including free surface and dry/wet bed. Additionally in many realistic engineering problems and flood forecasts, simplified mathematical models are usually adopted to compute the fluid flow. In contrast to three-dimensional Navier-Stokes equations (NSEs), one-dimensional river cross sectional area-averaged shallow water equations (SWEs) and two-dimensional depth-averaged SWEs use less computational resources during the numerical simulations. Since rivers are short and steep and the distributions of rainfall are uneven in seasons and regions in Taiwan, river discharges vary dramatically. This makes the flow conditions are challenging to predict. SPH is suitable for dealing with these situations due to its Lagrangian concept and particle nature. To date, there are numbers of models and solvers based on SPH-SWEs. However, an import issue still remains to be resolved. It comes from the restriction of



dimensions of SWEs. Unlike the 3D Navier-Stokes Equations, SWEs are 2D depth-averaged equations in the  $x$ - $y$  plane or 1D cross-section-averaged equations in the streamwise direction. Thus, there is no extra dimension which can be used for inputting/outputting fluids beyond the computational domain. It means that the current SPH-SWEs model cannot process the situations like lateral flow, rainfall, or infiltration. Therefore, a novel algorithm is developed using mass-varied fluid particles. This mass-varied SPH-SWEs model is able of conquering this difficulty and will be used to investigate the rainfall-runoff processes and infiltration. In addition, an 1D SPH sewer model is also constructed in this thesis. In future work, the SPH rainfall-runoff model and the SPH sewer model can integrate into a SPH flood model by means of fluid mass transfer between them. For example, when the runoff flows into sewers, the particle mass will decrease in the runoff and increase in the sewer. Or if a manhole occurs overflow the fluid and the particle mass will transfer from the sewers for the ground runoff.

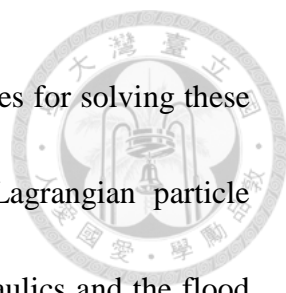
## **1.2 Research method and SPH**

In many hydraulic and environmental engineering problems, computational fluid dynamics (CFD) is used to analyze and predict the fluid motions in temporal and spatial domains numerically. According to observer's frame of references, CFD analysis has two concepts: the Lagrangian concept and the Eulerian concept. In Lagrangian concept



the observer follows an individual fluid parcel as it moves through space and time, while in Eulerian concept the observer focuses on specific locations in the space through which the fluid flows as time passes. Traditional CFD methods are usually based on Eulerian concept, e.g., finite difference method (FDM), finite element method (FEM) and finite volume method (FVM), etc. The foregoing methods discretize the computational domain with regular or irregular grids, and then utilize the difference formulas, the control volume integral and the technique of weighted residuals, respectively, to solve the fluid governing equations. However in some problems and situations, it is hard to apply Eulerian concept to describe the fluid motion with time passing on dealing with free surface, moving boundary, shock wave, supercritical/subcritical/transcritical flow, adverse flow, converge flow, overtopping flow, and dry-wet interface flow, etc. Otherwise, when considering the surrounding flow field of dam break, gate operation of hydraulic structures, pollution diffusion and flow field of tidal surges in the bay, the Eulerian grid-based methods also have large restrictions. It is because that the outside or inside boundaries of these problems are moveable instead of locking in fixed regions. The restriction of grid geometry and the moving inside/outside boundaries make that the numerical grid generation has to be changed with the boundary of the flow field accordingly. These are the difficulties to the traditional grid-based CFD methods.





On the contrary, the Lagrangian CFD methods are the candidates for solving these issues. Among them, SPH is one of the increasingly popular Lagrangian particle methods. In this research, SPH is used to investigate the river hydraulics and the flood overland flow. Initially SPH has been introduced for solving 3D physical problems of celestial bodies in open space (Lucy, 1977; Gingold and Monaghan, 1977). Afterwards, SPH are developed into an efficient computational model and implemented on the area of computational fluid dynamics. Different from the grid-based methods which need additional treatments for moving boundaries, SPH can handle these easily with its particle nature. The physical quantities are carried by the particles in the computational domain. When particles move under the control of the governing equations, the quantities also change accordingly. This solving algorithm can get rid of the restriction of fixed grids. The major concept of SPH is using approximated functions to construct the connections between particles. Therefore the computation of SPH is closer to the interpolation of FDM, and is more efficient than FVM and FEM but has the comparable accuracy. Thus SPH can be an alternative tool for simulating the flow fields with severe conditions, and has the potential for dealing with flow fields with complex boundaries. In summary, SPH has the following major advantages and disadvantages:

Advantages:



- (1) Physical domains are discretized by particles. Without the restriction of fixed grids, SPH can solve problems with complex boundaries and severe flow conditions; especially the solid-liquid two-phase flows.
- (2) Due to the Lagrangian nature, the free surface can be captured by SPH automatically and the dry-wet bed situation in open channel flow needs no special treatments.
- (3) The governing equations under the Lagrangian concept have only the time derivatives term but no convection terms. Therefore the numerical dispersion and oscillations can be evidently avoided.

Disadvantages:

- (1) When particles become over-cluster or over-scatter, the kernel will give the uneven weighting between particles during the computation. Therefore the accuracies of the results are affected.
- (2) SPH inconsistency: free surface particle near the boundary has the incomplete compact domain. This will cause the errors when doing the interpolation or differential operation and further influence the accuracies. More seriously it could lead to the numerical instability.
- (3) In the computing processes, SPH has to search the neighbor interaction particles for each particle and the interaction particles have to maintain a

certain number. Thus the particle searching algorithm will cost most computing time, sometimes it will slow down the efficiency when particle number becomes large.



### **1.3 Synthesis**

The content of this thesis is divided into seven chapters:

Chapter 1 includes the objectives, research method and synthesis.

Chapter 2 is the literature review.

Chapter 3 is the introduction of the SPH basic theory and the fundamental formulations.

Chapter 4 describes the discretization of SWEs, SPH-SWEs model, the solving processes and the setup of boundary conditions

Chapter 5 is the derivation of novel SPH model using mass-varied particles and the connection between the original and new approaches is also demonstrated.

Chapter 6 is the module studies, including rainfall-runoff processes, infiltration and sewer.

Chapter7 is the conclusions and suggestions.



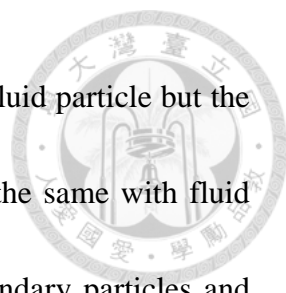
## Chapter 2 Literature review

### 2.1 SPH theory

Smoothed particle hydrodynamics (SPH) is a Lagrangian meshless method introduced by Lucy (1977) and Gingold and Monaghan (1977). Its major features are using particles instead of grids to discretize the physical domain and dealing with spatial derivative terms with particle weighting. Recently SPH has become increasingly popular and has the wide-ranged applications on kinds of fields, e.g. astrodynamics (Monaghan and Lattanzio, 1985), Magnetohydrodynamics (Borve *et al*, 2001; Price, 2012), solid mechanics (Libersky *et al.*, 1993; Bonet and Kulasegaram, 2000) and fluid dynamics (Monaghan, 1994; Monaghan, 2005), etc. To date, SPH has enormous developments on its basic theory, including boundary condition, fundamental formulations, efficiency, and error analysis, etc. The important literatures are listed as following:

#### 2.1.1 Wall boundary condition

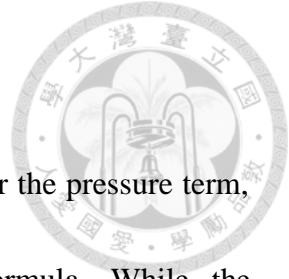
Monaghan (1994) used the solid boundary particles to impose the wall boundary conditions. These particles are fixed in certain positions. When the fluid particles are near the boundary, the solid boundary particles will give the repulsive force to prevent from the fluid particles flow through the wall boundary. Randles and Libersky (1996) proposed the mirror particles to represent the wall boundary. When the fluid particles flow near the boundary, another side of the boundary will generate the mirror particles.



The velocity of mirror particle has equal value with the velocity of fluid particle but the direction is reverse. Moreover, their density and pressure are also the same with fluid particles'. Ferrari et al (2009) combined the concepts of solid boundary particles and mirror particles. The wall boundary is also represented by solid boundary particles while when the fluid particles flow near the boundary, the virtual particles will be generated outside by point symmetry according to the solid boundary particle. These mirror particles have the similar features with the fluid particles, e.g. the velocity with same magnitude but reverse direction and the equal density and pressure.

### *2.1.2 Inflow and outflow boundary*

Liu and Liu (2003) applied the periodic boundary learned from molecular dynamics on SPH simulations for Poiseuille flow and Couette flow. The function of the periodic boundary is that if the fluid particles go through such boundary, they will reencounter the domain from the corresponding boundary, and their physical quantities, such as mass, velocity and density, will not be changed. Federico et al (2012) developed a in/outflow algorithm for SPH. Three kinds of particles are implemented: inflow particles, inner fluid particles and outflow particles. Inner fluid particle is controlled by governing equations and in/outflow particle is used to impose the in/outflow boundary conditions. This algorithm is successfully applied on the open channel flows, including different regimes of hydraulic jumps and flood flowing through bridge.



### 2.1.3 SPH formula modification

In order to exactly satisfy the linear and angular momentum for the pressure term, Monaghan (1988) derived the SPH antisymmetric gradient formula. While the symmetric gradient formula can exactly maintain the mass conservation when applying on the continuity equation. Bonet and Lok (1999) examined that if the equation of motion in variational form can satisfy the linear and angular momentum or not. They found that it conserves the linear momentum but the SPH gradient formula has to be modified for conserving the angular momentum. Thus they proposed the mixed correction modifying the kernel function and SPH gradient and divergence, and they also applied them on the free surface flows, such as dambreak flows and surges.

### 2.1.4 Particle searching

Liu and Liu (2003) proposed the all-pair searching to search the neighbor interaction particles in SPH. For a certain particle, this method has to do the searches in the whole domain and for all the particles. If there are  $N$  particles, the complexity of the method is  $O(N^2)$ . Rhoades (1992) introduced linked-list searching to enhance the searching efficiency. In linked-list searching, the computational domain is divided by small square cells with width  $2h$  ( $h$  is the smoothing length). The particle searching carries out for the eight neighbor cells and the center cell where the target particle locates. The complexity of the linked-list searching is  $O(N \log N)$  when there are total  $N$



particles.

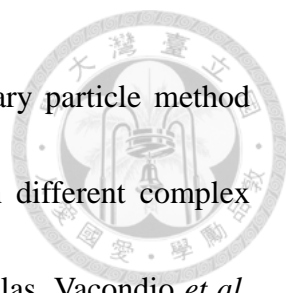
### 2.1.5 Error analysis

Quinlan *et al.* (2006) utilized Taylor expansion to analyze 1D SPH truncation error.

They concluded that the ratio of  $\Delta x/h$  (smoothing length  $h$ / particle spacing  $\Delta x$ ) is the important factor. Amicarelli *et al.* (2011) followed the research of Quinlan *et al.* (2006) analyzing the 3D SPH truncation error and derived the error formulas with polynomials of degree of zero, one and two.

## 2.2 SPH application on shallow water equations and SPH-SWEs model

Wang and Shen (1999) first applied SPH on solving SWEs and simulating the dambreak flows with wet-dry bed interface. Ata and Soulaïmani (2005) proposed the new artificial viscosity formula which is different from the one given by Monaghan (1988). This new formula does not include any parameters such as smoothing length or constant numbers. Thus the artificial viscosity does not need to be tuned case by case and can also avoid producing the numerical oscillations due to the inappropriate setups of parameters. They applied this new viscosity formula on simulating the dambreak flows with wet bed. Rodriguez-Paz and Bonet (2005) derived the variational form of SWEs to describe the motion of shallow water wave and used the iteration to solve the nonlinear SPH summation depth formula. They also conducted the simulations of dam break with channel cross sections. De Leffe *et al.* (2010) solved the dambreak flows and




soliton waves. Vacondio et al (2012b) modified the virtual boundary particle method introduced by Ferrari et al (2009) and simulated flow fields with different complex boundary geometries by using variational form of SPH-SWEs formulas. Vacondio *et al.* (2011; 2012a; 2012b) improved the closed boundary conditions of SPH with the use of virtual particles, enhanced the resolution of the small depth problems by using the particle splitting process with shock capturing method, and introduced the open boundary treatment considering the Riemann states. Chang *et al.* (2011) and Kao and Chang (2012) applied SPH on shallow-water dambreak flows in open channels and floodplains. Jian *et al.* (2015) and Pu *et al.* (2013) further developed the numerical modeling techniques for dambreak flows with SPH. Chang and Chang (2013) investigated non-rectangular and non-prismatic open channel flows with a novel specified interval time method of SPH-SWEs. In general, these SPH researches have targeted on rapidly-varying flows with steep velocity gradients such as transient or dambreak flows (Chang and Chang, 2017).

### **2.3 Rainfall-runoff processes and models**

The rainfall-runoff process is an important hydrological phenomenon that relates the stream flow response of a river to a given amount of rainfall (Beven, 2001). Rainfall-runoff modeling can be classified into two major categories based on the hydrologic system: black box lumped modeling and physically based distributed






modeling (Chow *et al.*, 1988). Lumped modeling averages parameters for the entire watershed, ignores flow-routing mechanisms, and transforms effective rainfall into an outflow hydrograph. It can quickly obtain results, but cannot provide detailed physical processes (Freeze and Harlan, 1969). Distributed modeling considers variations in variables and parameters based on understanding different physical processes. It solves the shallow water equations (SWEs) computationally using the fully dynamic wave approach or the simplified forms of the SWEs using the diffusive wave approximation or the kinematic wave approximation. A variety of numerical methods have been used to solve rainfall-runoff problems, including finite difference methods (Esteves *et al.*, 2000; Fiedler and Ramirez, 2000), finite volume methods (Cea *et al.*, 2010; Costabile *et al.*, 2013), and finite element methods (Vieux and Gauer, 1994).

## 2.4 Infiltration


Woolhiser *et al.* (1996) solved the Smith-Parlange infiltration model by using finite difference scheme on a characteristic computational net and showed that runoff hydrographs are strongly affected by trends in hydraulic conductivity, particularly for small runoff events. A model based on the MacCormack finite difference scheme with spatially variable infiltration was presented by Fiedler and Ramirez (2000). They simulated infiltration with Green-Ampt model coupled to the surface water component that allows dynamic interaction. Esteves *et al.* (2000) used an explicit finite difference



scheme and demonstrated that the best simulation results of infiltration were obtained by using calibrated values of the wetting front pressure. However their scheme needed a special treatment for preventing negative water depths. Liu *et al.* (2004) thought that fully 2D dynamics model was hard to implement because of thin water depth and complex surface boundaries. Therefore they developed a 2D kinetic wave model for simulating runoff generation on experimental infiltrating hillslope with Green-Ampt model. Chahinian *et al.* (2005) compared four different infiltration models to simulate flood events at the field scale: Philip, Morel-Seytoux, Horton and SCS. They concluded that Morel-Seytoux's model is better and the results also revealed the issues related to the simulations of low flow events and intermittent rainfall events. Chen and Young (2006) extended Green-Ampt equation onto sloping surfaces and found that the slope effect is important for low-intensity and short duration rainfall events with ponded infiltration. Their results also showed that infiltration increases with increasing slope angle. In order to preserve the depth-positivity, Singh *et al.* (2014) proposed a model based on the 2D fully nonlinear SWEs solved by using a second-order central-wind shock-capturing scheme and the tempospatial variation of rainfall intensity and infiltration are taken into account as source and sink terms.

## **2.5 Drainage systems and sewers**

Since that Preissmann slot method (PSM) suffers from the inability of describing



subatmospheric full-pipe flows, Vasconcelos *et al* (2006a) presented a new approach utilizing a shock-capturing technique that decouples the hydraulic pressure from surcharged pressures occurring only in pressurized conditions. Thus this approach is named two-component pressure approach (TPA). The feature of TPA is that it exploits the identity between the incompressible flow equations for elastic pipe walls and SWEs. With TPA only minor modification is required for solving the surcharge flows and free surface flows at the same time with one single governing equation (Vasconcelos and Wright, 2007; Vasconcelos and Marwell, 2011; Bousso *et al.* 2013). Sanders *et al.* (2011) improved the numerical model of TPA to support storm sewer network simulations and enabled it to couple with a 2D overland flow model. Bourdarias and Gerbi (2007) also developed a model with finite volume scheme for free surface and pressurized flows. In their model the transition point between the two types of flows is treated as a free boundary associated to a discontinuity of the gradient pressure. Although they derived the model with flux integral, the final form of the governing equation is identical to the model of TPA. Casulli and Stelling (2013) proposed a semi-implicit numerical model for urban drainage system. Their model is robust and accurate and can deal with the occurrence of dry areas because the governing equations are discretized with the consistent mass conservative scheme. However when encountering the complex flow conditions, this model would be inefficient due to the two-layer iteration algorithm and

the solving process of Poisson pressure equation.





## Chapter 3 Theories and Methods

### 3.1 Introduction of SPH

SPH is a meshfree method with Lagrangian description, which guarantees the conservation of momentum and mass. SPH particles are not only interpolation points but also carry material properties like real physical objects. In SPH, particles are used to discretize the computational domain (called *particle representation*) and the interaction among particles is connected by the use of the weighting kernel function. Governing equations in SPH is first represented by integral representation and discretized by *particle approximation* thereafter. Numerical algorithm updates the particles' motions together with the physical quantities in each step. Therefore the solutions of the problems are obtained steps by steps.

### 3.2 Central concept and fundamental formulations

The central concept of SPH comes from integral representation and interpolation.

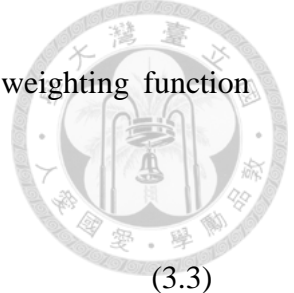
An arbitrary function  $f(\mathbf{x})$  can be written as an integral form

$$f(\mathbf{x}) = \int_{\Omega} f(\mathbf{x}') \delta(\mathbf{x} - \mathbf{x}') d\mathbf{x}' \quad (3.1)$$

where

$$\delta(\mathbf{x} - \mathbf{x}') = \begin{cases} \infty, & \mathbf{x} = \mathbf{x}' \\ 0, & \mathbf{x} \neq \mathbf{x}' \end{cases} \quad (3.2)$$

is the Dirac delta function.



After replacing the delta function  $\delta(\mathbf{x} - \mathbf{x}')$  with a smoothing weighting function  $W(\mathbf{x} - \mathbf{x}', h)$ , the integral representation of  $f(\mathbf{x})$  is

$$f_I(\mathbf{x}) = \int f(\mathbf{x}')W(\mathbf{x} - \mathbf{x}', h)d\mathbf{x}' \quad (3.3)$$

The function  $W(\mathbf{x} - \mathbf{x}', h)$  should satisfy the following conditions:

1. Normalization condition/unity condition

$$\int_{\Omega} W(\mathbf{x} - \mathbf{x}', h)d\mathbf{x}' = 1 \quad (3.4)$$

2. Delta function property

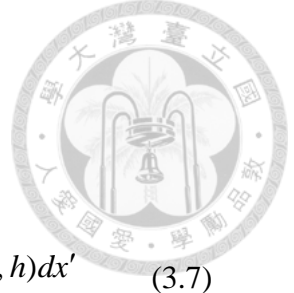
$$\lim_{h \rightarrow 0} W(\mathbf{x} - \mathbf{x}', h) = \delta(\mathbf{x} - \mathbf{x}') \quad (3.5)$$

3. Compact condition

$$W(\mathbf{x} - \mathbf{x}', h) = 0, \quad \text{if } |\mathbf{x} - \mathbf{x}'| > \kappa h \quad (3.6)$$

where  $\kappa$  is a constant related to the radius of the smoothing function for the point at  $\mathbf{x}$  (usually choose  $\kappa = 2$ ). The effective region of the smoothing weighting function  $W$  is called the support domain of particle in SPH and  $W$  is also known as the kernel weighting function. By using this compact condition, the integration over the entire computational domain can be localized as integrating over the support domain of the smoothing function. Thus, the integration of the entire computational domain can be changed into the integration of support domain as shown in Figure 3.1.

In general, the errors of integral representation in SPH can be estimated as follows. After expanding  $f(\mathbf{x}')$  in a Taylor series about  $\mathbf{x}'$  and keeping up to second order



terms, we can obtain

$$\begin{aligned}
 f_I(\mathbf{x}) &= \int_{\Omega} [f(\mathbf{x}) + f'(\mathbf{x})(\mathbf{x} - \mathbf{x}') + O((\mathbf{x} - \mathbf{x}')^2)] W(\mathbf{x} - \mathbf{x}', h) d\mathbf{x}' \\
 &= [f(x) + O(h^2)] \int_{\Omega} W(x - x', h) dx' + f'(x) \int_{\Omega} (x - x') W(x - x', h) dx' \quad (3.7)
 \end{aligned}$$

Because  $W$  is an even function and satisfies the unity condition, we have

$$f_I(\mathbf{x}) = f(\mathbf{x}) + O(h^2) \quad (3.8)$$

which shows that the integral representation has a second order accuracy.

### 3.3 Particle approximation

A particle  $j$  with a density  $\rho$  and a small volume  $\Delta V$  has the mass

$$m_j = \Delta V_j \rho_j. \quad (3.9)$$

Substituting this relationship to transform the continuous integral representation of

$f(\mathbf{x})$  into the particle approximation gives

$$\begin{aligned}
 f(\mathbf{x}) &= \int_{\Omega} f(\mathbf{x}') W(\mathbf{x} - \mathbf{x}', h) d\mathbf{x}' \\
 &= \sum_{j=1}^N f(\mathbf{x}_j) W(\mathbf{x} - \mathbf{x}_j, h) \Delta V_j \\
 &= \sum_{j=1}^N f(\mathbf{x}_j) W(\mathbf{x} - \mathbf{x}_j, h) \frac{m_j}{\rho_j}. \quad (3.10)
 \end{aligned}$$

Thus,

$$f_I(\mathbf{x}_i) = \sum_{j=1}^N \frac{m_j}{\rho_j} f(\mathbf{x}_j) W(\mathbf{x} - \mathbf{x}_j, h). \quad (3.11)$$

This equation states that the value of a field function for the particle  $i$  is approximated

by a summation over all the particles in the support domain. The kernel function  $W$  is



associated to the distances between particles.

For example, taking  $f_i(\mathbf{x})$  as the density  $\rho(\mathbf{x})$ , Eq. (3.11) gives the following estimate for the density for particle  $i$  at the position  $\mathbf{x}$

$$\rho_i(\mathbf{x}) = \sum_j m_j W(\mathbf{x} - \mathbf{x}_j, h). \quad (3.12)$$

If  $h$  is constant, we can integrate this estimate and obtain the following statement

$$\int \rho(\mathbf{x}) dV = \sum_i \sum_j m_j W(\mathbf{x} - \mathbf{x}_j, h) = \sum_i m_i = M \quad (3.13)$$

or

$$M = \sum_j W(\mathbf{x} - \mathbf{x}_j, h) \frac{m_j}{\rho_j} = \text{constant} \quad (3.14)$$

which describes that the total mass is exactly conserved. However, in some situations,  $h$  is variable, so the integral is not exactly equal to  $M$ . However the mass conservation is still satisfied because of the conservation of particle number. See the later section for illustration.

### 3.4 Derivation of fundamental formulations

There are three approaches to derive the SPH interpolation formulation:

1. Integral approach (Liu and Liu, 2003)
2. Derivative approach (Monaghan, 2005)
3. Variation approach (Bonet *et al.*, 2004)

In this thesis, we follow Monaghan's steps to derive the SPH formulation because it is





more intuitional than the others.

### 3.4.1 First derivative

If  $W$  is a differentiable function, then we differentiate Eq. (3.11) to get

$$\frac{\partial f}{\partial x} = \sum_j \frac{m_j}{\rho_j} f_j \frac{\partial W}{\partial x} \quad (3.15)$$

where  $f(\mathbf{x}_j)$  is denoted by  $f_j$ . If  $f$  is a constant, the LHS of Eq. (3.15) vanishes, but

the RHS of Eq. (3.15) does not. Thus, we apply the following identity equation to Eq.

(3.15) to ensure the RHS of Eq. (3.15) does vanish if  $f$  is constant

$$\frac{\partial f}{\partial x} = \frac{1}{\phi} \left( \frac{\partial(\phi f)}{\partial x} - f \frac{\partial \phi}{\partial x} \right) \quad (3.16)$$

where  $\phi$  is any differentiable function, and Eq.(3.15) becomes

$$\left( \frac{\partial f}{\partial x} \right)_i = \frac{1}{\phi_i} \sum_j \frac{m_j}{\rho_j} \phi_j (f_j - f_i) \frac{\partial W_{ij}}{\partial x_i} \quad (3.17)$$

where  $W_{ij}$  denotes  $W(\mathbf{x}_i - \mathbf{x}_j, h)$ . Above equation vanishes if  $f$  is constant. There are two

choices of  $\phi$  that can obtain the two versions of SPH first derivative formulation. For

example, choosing  $\phi = 1$  we can get

$$\left( \frac{\partial f}{\partial x} \right)_i = \sum_j \frac{m_j}{\rho_j} (f_j - f_i) \frac{\partial W_{ij}}{\partial x_i} \quad (3.18)$$

and choosing  $\phi = \rho$  that gives

$$\left( \frac{\partial f}{\partial x} \right)_i = \frac{1}{\rho_i} \sum_j m_j (f_j - f_i) \frac{\partial W_{ij}}{\partial x_i} \quad (3.19)$$

Eq. (3.18) and Eq. (3.19) are the two different forms of SPH gradient operator which



can also be written as

$$(\nabla f)_i = \frac{1}{\rho_j} \left[ \sum_j^N m_j [f(x_j) - f(x_i)] \nabla_i W_{ij}^i \right] \quad (3.20)$$

$$(\nabla f)_i = \rho_i \left[ \sum_j^N m_j \left[ \frac{f(x_j)}{\rho_j^2} + \frac{f(x_i)}{\rho_i^2} \right] \nabla_i W_{ij}^i \right] \quad (3.21)$$

Eq. (3.20) is an antisymmetric form for particle  $i$  while Eq. (3.21) is a symmetric form for particle  $i$  (Liu and Liu, 2003). Eq. (3.20) is used to calculate the gradient of bottom elevation because  $\nabla b$  should be zero when the terrain is flat ( $b = \text{constant}$ ). Eq. (3.21) is used to calculate the inter force term  $\mathbf{T}$  (see section 4.4) due to its local conservation properties and intrinsic remeshing procedure (Price, 2012).

### 3.4.2 Second derivative

To derive the second derivative, we start with an integral approximation (Cleary and Monaghan, 1999):

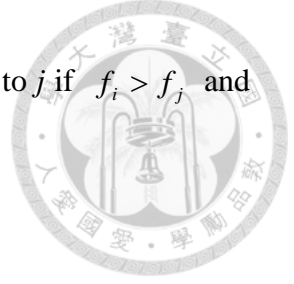
$$I = \nabla \cdot (D \nabla f) + O(h^2) = \int (D(\mathbf{x}) + D(\mathbf{x}')) (f(\mathbf{x}) - f(\mathbf{x}')) F(\mathbf{x} - \mathbf{x}') dx' \quad (3.22)$$

where  $\mathbf{q}F(\mathbf{q}) = \nabla W(\mathbf{q})$  and  $D$  represents the diffusion coefficient function. The SPH particle discretization form of  $I$  is

$$I = \sum_j \frac{m_j}{\rho_j} (D_i + D_j) (f_i - f_j) F_{ij} \quad (3.23)$$

or

$$\nabla \cdot (D \nabla f) = \sum_j \frac{m_j}{\rho_j} (D_i + D_j) (f_i - f_j) F_{ij} \quad (3.24)$$



Because  $F_{ij} \leq 0$  the physical quantity  $f$  will transfer from particle  $i$  to  $j$  if  $f_i > f_j$  and vice versa.

### 3.5 The choices of kernel functions

There are many kinds of kernel functions adopted from the previous studies. We just list three types commonly used as followings. Here,  $q = \frac{r}{h} = \frac{|\mathbf{x} - \mathbf{x}'|}{h}$ .

1) Gaussian kernel :

$$W(q, h) = \alpha_d \exp(-q^2) \quad (3.25)$$

where  $\alpha_d$  is  $1/(\pi^{1/2}h)$  in 1D and  $1/(\pi h^2)$  in 2D.

2) Quadratic kernel:

$$W(q, h) = \alpha_d \left[ \frac{3}{16} q^2 - \frac{3}{4} q + \frac{3}{4} \right] \quad 0 \leq q \leq 2 \quad (3.26)$$

where  $\alpha_d$  is  $1/h$  in 1D and  $2/(\pi h^2)$  in 2D.

3) Cubic spline:

$$W(q, h) = \alpha_d \begin{cases} \frac{2}{3} - q^2 + \frac{1}{2} q^3 & 0 \leq q < 1 \\ \frac{1}{6} (2 - q)^2 & 1 \leq q < 2 \\ 0 & q \geq 2 \end{cases} \quad (3.27)$$

where  $\alpha_d$  is  $1/h$  in 1D and  $15/(7\pi h^2)$  in 2D. In this thesis, we always use cubic spline for the kernel function. According to Monaghan (2005), although the higher order kernels perform well for equi-spaced particles, the features of positive definite dissipation terms in SPH are lost due to the sign changes of the gradient of the higher

order kernels. Fulk and Quinn (1996) and Price and Monaghan (2004) also found that in one dimension the cubic spline is a better kernel. Thus we adopt the cubic spline kernel for the purposes and implements.



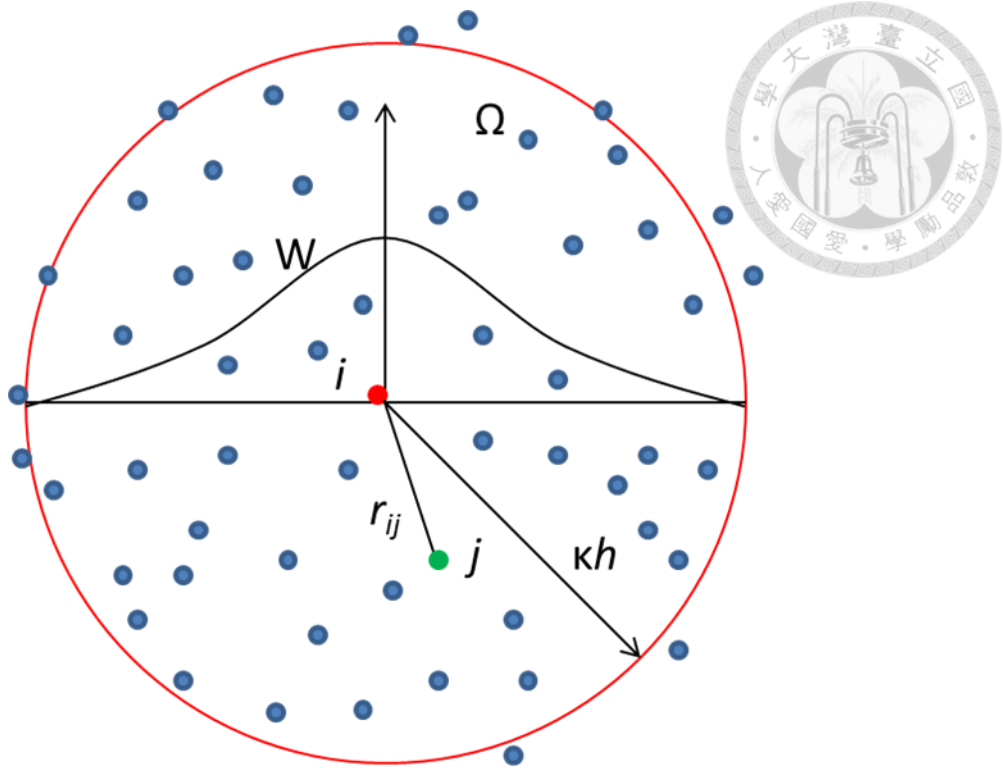


Fig. 3.1 Particle approximation (Liu and Liu, 2003)



## Chapter 4 SPH for shallow water equations and numerical techniques

The Navier-Stokes equations in the Lagrangian nonconservation form is

$$\frac{D\mathbf{v}}{Dt} = -\frac{1}{\rho}\nabla P + \mathbf{g} + \mathbf{\Theta} \quad (4.1)$$

$$\frac{D\rho}{Dt} = -\rho\nabla \cdot \mathbf{v} \quad (4.2)$$

$$\frac{D\mathbf{x}}{Dt} = \mathbf{v} \quad (4.3)$$

where  $\mathbf{\Theta}$  denotes the viscous diffusion term. In addition, for solving the thermodynamic problems, the fluid flow dynamic system will involve additional equations, for example, equation of state, energy/entropy equation or mass transfer equation, etc.

### 4.1 Shallow water equations and SPH-SWEs

Shallow water equations (SWEs) are derived by integrating the Navier-Stokes equations over the flow depth, as

$$\int_{z_b}^z \left\{ \begin{array}{l} \frac{D\rho}{Dt} = -\rho\nabla \cdot \mathbf{v} \\ \frac{D\mathbf{v}}{Dt} = \mathbf{g} - \frac{1}{\rho}\nabla P + \frac{\mu}{\rho}\nabla^2 \mathbf{v} \end{array} \right\} dz \quad (4.4)$$

in which  $Z$  and  $Z_b$  are the levels of the water surface and the channel bottom respectively.

A uniform velocity profile is assumed in the vertical direction. The viscous diffusion term is computed by  $\mathbf{\Theta} = \nu_0 \nabla^2 \mathbf{v}$  here, and  $\nu_0$  is the kinetic viscosity of laminar flow.

The use of SWEs has two main advantages. One is that the  $N$  dimension Navier-Stokes equations are equivalent to  $N-1$  dimension shallow water equations. The



other one is that the shallow water equations can bring the effect of terrain into consideration through the bed gradient source term. Therefore, we can use the SPH-SWEs to simulate the natural rivers, hydraulic structures and ocean, macroscopic fluid flow, and ground flow phenomena.

In SPH-SWEs each particle represents a water column. The height of the water column is the water depth  $d_w$ , which is the distance between the free water surface level and the bottom bed level. These particles at the  $x$ - $y$  plane move according to the topography of the terrain described by  $b(x, y)$  as shown in Figure 4.1. For implementing SWEs, two assumptions should be considered. One is that the velocity on the vertical direction of the bottom,  $v_z$ , is small. This means that the instantaneous spatial variation of  $d_w$  is small. The  $z$  position of the bottom of each column can be given by

$$z = b(x, y) \quad (4.5)$$

Differentiated with respect to time, the vertical velocity can be evaluated as

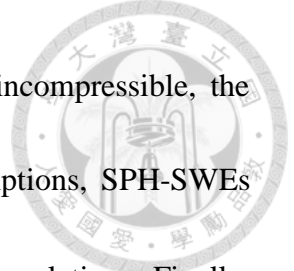
$$\frac{\partial z}{\partial t} = \frac{\partial b}{\partial x} \cdot \frac{\partial x}{\partial t} + \frac{\partial b}{\partial y} \cdot \frac{\partial y}{\partial t} \quad (4.6)$$

$$v_z = \nabla b \cdot \mathbf{v} \quad (4.7)$$

where  $\mathbf{v} = (u, v)$  is the velocity of the water column projected onto the corresponding particle on 2D  $x$ - $y$  plane (see Fig. 4.1). Another assumption is that

$$\rho = \rho_w d_w \quad (4.8)$$

where  $\rho_w$  denotes the constant 3D density of fluid, and  $\rho$  means the 2D projecting



density of the fluid. Because the fluid motion is assumed to be incompressible, the water density  $\rho_w$  is uniform and constant. With these two assumptions, SPH-SWEs can be derived analogous to the standard 2D SPH interpolation formulations. Finally, the SWEs can be written as follows:

$$\frac{D\rho}{Dt} = -\rho \nabla \cdot \mathbf{v} \quad (4.9)$$

$$\frac{D\mathbf{v}}{Dt} = -\frac{g}{\rho_w} \nabla \rho + g(-\nabla b - \mathbf{S}_f) \quad (4.10)$$

where  $\mathbf{v} = (u, v)$  is the velocity vector on  $x$ - $y$  plane,  $b$  is the bottom elevation,  $g$  is the gravity acceleration and  $\mathbf{S}_f$  is the friction source term. Because of the hydrostatic assumption applied herein, the shallow water equations need no additional state equations to solve the dynamic pressure. And the last two terms,  $b$  and  $\mathbf{S}_f$ , can be regarded as the force source terms and play important roles when dealing with problems in natural rivers or irregular channels. In SPH-SWEs, Eq. (4.9) and Eq. (4.10) are always rewritten as following  $u$ - $d_w$  form with the relationship Eq. (4.8):

$$\frac{Dd_w}{Dt} = -d_w \nabla \cdot \mathbf{v} + (R - f) \quad (4.11)$$

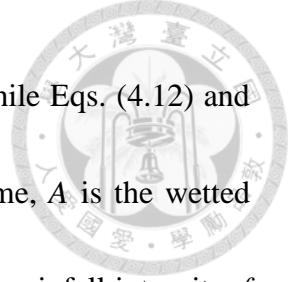
$$\frac{D\mathbf{v}}{Dt} = -g \nabla d_w + g(-\nabla b - \mathbf{S}_f) \quad (4.12)$$

In this thesis, the Q-A form of SWEs is also used for the simulations of 1D rivers and 1D sewers (Kao and Chang, 2012):

$$\frac{DA}{Dt} = -A \frac{\partial}{\partial x} \left( \frac{Q}{A} \right) + (R - f) \quad (4.13)$$

$$\frac{DQ}{Dt} = -Q \frac{\partial}{\partial x} \left( \frac{Q}{A} \right) - gA \frac{\partial d_w}{\partial x} + gA(S_0 - S_f) \quad (4.14)$$





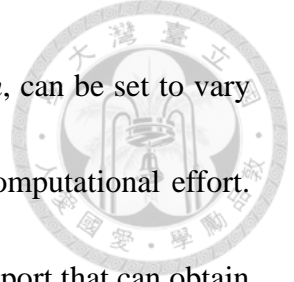
In the above, Eqs. (4.11) and (4.13) are the continuity equations, while Eqs. (4.12) and (4.14) are the momentum equations. In these equations,  $t$  is the time,  $A$  is the wetted cross-section area,  $Q$  is the discharge,  $d_w$  is the water depth,  $R$  is the rainfall intensity,  $f$  is infiltration rate,  $\mathbf{v}$  is the horizontal velocity vector ( $=\mathbf{v}(u, v)$ ),  $u$  is the  $x$ -component of  $\mathbf{v}$ ,  $v$  is the  $y$ -component of  $\mathbf{v}$ ,  $S_0$  is the bed slope,  $b$  is the bottom elevation,  $S_f$  ( $S_f$ ) is the friction slope, which is calculated according to either Manning's friction law (Kao and Chang, 2012; Chang and Chang, 2013) or the Darcy-Weisbach friction law (Delestre *et al.*, 2009), and  $g$  is the gravitational acceleration.

## 4.2 Water depth/cross-section wetted area evolution

As mentioned before, in SPH, the scale function  $f(\mathbf{x})$  can be approximated as follows:

$$f_i = \sum_j^N \frac{m_j}{\rho_j} f_j W_{ij}^i \quad (4.15)$$

where  $m_j$  is the mass of particle  $j$  ( $=\Delta x_0 \cdot \rho_j$  in 1D and  $\Delta x_0 \cdot \Delta y_0 \cdot \rho_j$  in 2D);  $\Delta x_0$  and  $\Delta y_0$  are the initial particle spacings in the  $x$ - and  $y$ -directions, respectively;  $\rho_j$  is the density of particle  $j$  defined as  $\rho_w \cdot A$  in 1D and  $\rho_w \cdot d_w$  in 2D;  $\rho_w$  is the constant water density (1000 kg/m<sup>3</sup>);  $N$  is the number of particles within the support domain of particle  $i$ ;  $W_{ij}^i$  is the kernel function; and  $\nabla_i W_{ij}^i$  is the first derivative of the kernel function.



On the other hand, in some simulation, the smoothing length,  $h$ , can be set to vary in some region domain in order to enhance the resolution or the computational effort. For large smoothing length, there are more particles in the kernel support that can obtain more accurate results. On the contrary, for small smoothing length, there are fewer particles in the support domain, which can speed up the computing. The smoothing length is updated according to the density (Benz, 1990):

$$h_i = h_{0,i} \left( \frac{\rho_{0,i}}{\rho_i} \right)^{1/D_m} \quad (4.16)$$

where  $\rho_{0,i}$ ,  $h_{0,i}$  are the initial density and smoothing length of the  $i$ -th particle, respectively, and  $D_m$  is the number of dimensions ( 1 in 1D and 2 in 2D ).

The variations of the projecting density  $\rho$  responds to the variations of water depth  $d_w$ . When the fluids exhibit the expansions or contractions, the density  $\rho$  may vary enormously. To keep the number of neighbor particles and mass roughly constant, the varying smoothing length scheme is therefore used. Instead of solving the continuity equation explicitly this scheme uses Eq. (4.17) as the mass constrain for stability reason by substituting  $\rho$  into Eq. (4.15) (Rodriguez-Paz and Bonet, 2005)

$$\rho_i = \sum_j m_j W_i(\mathbf{x}_j, h_i) \quad (4.17)$$

Eq. (4.17) is nonlinear due to the dependency of  $h_i$  on  $\rho_i$  (Eq. (4.16)). A simple Newton-Raphson iteration is used to solve this system. First, defining a residual



$Res(\rho_i^{(k)})$  for the  $k$ -th iteration of the density

$$Res(\rho_i^k) = \rho_i^k - \sum_j m_j W_i(\mathbf{x}_j, h_i) \quad (4.17)$$

in which the smoothing length evolves according to

$$h_i^{(k)} = h_{0,i} \left( \frac{\rho_{0,i}}{\rho_i^{(k)}} \right)^{1/D_m} \quad (4.18)$$

Using Newton-Raphson iterative formula

$$\rho_i^{k+1} = \rho_i^k - \frac{Res_i^k}{\left( \frac{dRes}{d\rho} \right)_i} = \rho_i^k - \frac{\rho_i^k - \sum_j m_j W_i(\mathbf{x}_j, h_i^k)}{\left( \frac{dRes}{d\rho} \right)_i} \quad (4.19)$$

where the derivative of the residual is calculated by using the chain rule

$$\begin{aligned} \frac{dRes}{d\rho} &= 1 - \sum_j m_j \frac{dW_i}{dh_i} \frac{dh_i}{d\rho_i} \\ &= 1 + \sum_j \frac{m_j}{\rho_i d_m} \left( W_i d_m + r_{ij} \frac{dW_i}{dr_{ij}} \right) \\ &= 1 - \frac{1}{\rho_i} \sum_j m_j W_i(\mathbf{x}_j, h_i) + \frac{\alpha_i}{d_m \rho_i} \end{aligned} \quad (4.20)$$

where  $\alpha_i$  is a correction factor that arises with the variable- $h$  formulation (Bonet *et al.*, 2004), and  $r_{ij} = |\mathbf{x}_i - \mathbf{x}_j|$ .

$$\alpha_i = - \sum_j m_j r_{ij} \frac{dW_i}{dr_{ij}} \quad (4.21)$$

After substituting Eq. (4.19) and Eq. (4.20) into Eq. (4.19), the equation becomes

$$\rho_i^{k+1} = \rho_i^k \left( 1 - \frac{Res_i^k d_m}{Res_i^k d_m + \alpha_i^k} \right) \quad (4.22)$$

The iterative procedure will complete and achieve the convergence when

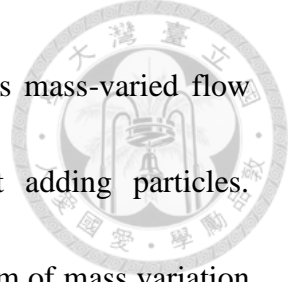
$$\frac{|Res_i^{k+1}|}{\rho_i^k} \leq \varepsilon \quad (4.23)$$



is satisfied. Taking  $\varepsilon = 10^{-10}$  allows the convergence being reached within a few iterations. The solving processes of the  $Q$ - $A$  form of SWEs are similar and it can refer to Chang and Chang (2013).

### 4.3 Using mass-varied particles and the modified smoothing length updating formulation

Some difficulties are associated with using SPH to solve SWEs. Unlike the 3D Navier-Stokes Equations, SWEs are 2D depth-averaged equations in the  $x$ - $y$  plane or 1D cross-section-averaged equations (also called the Saint-Venant equations) in the streamwise direction  $l$ . Thus, no dimension exists for vertical rainfall inputs. Therefore, mass-varied particles are used in the SPH-SWEs in this study to overcome this issue when modeling the model rainfall-runoff process. Figure 4.2 illustrates the concept of how mass-varied particles work. In modeling discharge flows without rainfall, river flows are discretized with water slide particles using a 1D SPH method (Chang *et al.*, 2011), while surface overland flows are discretized with water column particles using a 2D SPH method (Kao and Chang, 2012) (both are presented in blue in Fig. 4.2b). As rainfall occurs, the additional masses are added to the water slides or columns according to the product of their bottom area and the variation in water depth (presented in orange



in Fig. 4.2b). With this new treatment, the SPH-SWEs can address mass-varied flow fields, such as rainfall, infiltration, lateral flows, etc., without adding particles. Furthermore, this treatment does not need to construct the source term of mass variation in advance, which is helpful for encoding.

As previously discussed, no extra dimension is available to input rainfall particles when modeling the rainfall-runoff process based on SWEs using traditional methods. However, the rainfall process can be simulated by altering the water depth (which is the particle density  $\rho$ ) of each particle. Note that if we treat the particle mass as a constant value, the mass and momentum conservation of each particle cannot be achieved simultaneously because the mass and momentum of the raindrop adds to the system. Thus, the particle mass should be varied.

To reflect the rainfall effect on the evolution of the water depth of a fluid particle, we transform the rainfall amount into the increase of the mass of a fluid particle ( $\Delta m$ ) based on Eq. (4.24):

$$\Delta m = \rho \Delta V = \rho_w \Delta d_w \Delta V = \rho_w R \Delta t \Delta V \quad (4.24)$$

where  $V$  is the particle volume ( $= m/\rho$ ) and  $\Delta t$  is the time step.

However, the use of mass-varied fluid particles violates the assumption of constant mass in Eq. (4.16). We further assess the consequence of using Eq. (4.16) under the scenario of using fluid particles with varying mass in Fig. 4.3. When there is no rainfall,



the smoothing length of particle  $i$  updated according to Eq. (4.16) decreases as the water depth of particle  $i$  is increased to keep the number of fluid particles within the support domain of particle  $i$  fixed (as shown by comparing Fig. 4.3a and b). If rainfall occurs, the support domain decreases (by comparing Fig. 4.3a and c). However, at this instant there are fewer fluid particles in the support domain of particle  $i$  because Eq. (4.16) assumes that the total particle mass is constant in the support domain. The insufficient number of neighboring particles due to the inappropriately small smoothing length leads to numerical instability in the calculation of particle density. Therefore, we aim to derive a new formulation that updates the smoothing lengths of fluid particles in this study.

First, the particle number within the support domain of particle  $i$  is calculated using Eq. (4.25) (Violeau, 2012):

$$\bar{N} = \frac{\lambda_{D_m} h_i^{D_m}}{V_i} \quad (4.25)$$

where  $V_i$  is the volume of particle  $i$ ,  $\lambda_{D_m}$  is constant ( $\lambda_1 = 2$  and  $\lambda_2 = \pi$ ) and  $\bar{N}$  is the average particle number within the support domain of each fluid particle. Then, we assume that the particle number ( $\bar{N}$ ) within the support domain of particle  $i$  is constant, as shown in Eq. (4.26).

$$\frac{d\bar{N}}{dt} = \frac{d}{dt} \left( \frac{\lambda_{D_m} h_i^{D_m}}{V_i} \right) = 0 \quad (4.26)$$

From Eq. (4.26), we can obtain an equivalent equation as follows:



$$\frac{\lambda_{D_m} h_{0,i}^{D_m}}{V_{0,i}} = \frac{\lambda_{D_m} h_i^{D_m}}{V_i} \quad (4.27)$$

where  $V_{0,i}$  is the initial volume of particle  $i$ . After rearranging Eq. (4.27), the new formulation for updating the smoothing lengths of fluid particles can be presented as follows.

$$h_i = h_{0,i} \left( \frac{V_i}{V_{0,i}} \right)^{1/D_m} \quad (4.28)$$

Note that Eq. (4.28) is identical to Eq. (4.16), as the particle mass remains constant.

Two approaches for determining the water depths (wetted cross-section areas) of fluid particles, including solving the coupled system of Eqs. (4.17) and (4.28) and solving the continuity equations of Eqs. (4.11) and (4.13), have been compared. We aim to show the connection between the SPH summation operator of particle density and the SPH approximation of the continuity equation for mass-varied particles. First, Eq. (4.28) becomes Eq. (4.29) by differentiating with respect to  $\rho$ .

$$\begin{aligned} \frac{dh_i}{d\rho_i} &= \frac{\partial}{\partial \rho_i} \left[ h_{0,i} \left( \frac{m_i}{m_{0,i}} \frac{\rho_0}{\rho_i} \right)^{1/D_m} \right] \\ &= h_{0,i} \left( \frac{m_i}{m_{0,i}} \right)^{1/D_m} \frac{d}{d\rho_i} \left( \frac{\rho_0}{\rho_i} \right)^{1/D_m} \\ &= h_{0,i} \left( \frac{m_i}{m_{0,i}} \right)^{1/D_m} \left( \frac{\rho_0}{\rho_i} \right)^{1/D_m} \left( -\frac{1}{D_m \rho_i} \right) \\ &= -\frac{h_i}{D_m \rho_i} \end{aligned} \quad (4.29)$$



Using the chain rule for the smoothing length and applying Eq. (4.29) leads to the following expression.

$$\frac{dh_i}{dt} = \frac{dh_i}{d\rho_i} \frac{d\rho_i}{dt} = -\frac{h_i}{D_m \rho_i} \frac{d\rho_i}{dt} \quad (4.30)$$

Next, we take the time derivative of Eq. (4.17) to obtain the following equation.

$$\frac{d\rho_i}{dt} = \sum_j^N m_j \left[ \frac{dW_{ij}^i}{dr_{ij}} \frac{dr_{ij}}{dt} + \frac{dW_{ij}^i}{dh_i} \frac{dh_i}{dt} \right] + \sum_j^N \frac{dm_j}{dt} W_{ij}^i \quad (4.31)$$

Substituting Eq. (4.30) into Eq. (4.31) and applying the following equations (Eqs. (4.32)

and (4.33)), Eq. (4.31) can be rewritten as Eq. (4.34):

$$\frac{dW_{ij}^i}{dr_{ij}} \frac{dr_{ij}}{dt} = \frac{dW_{ij}^i}{dr_{ij}} \cdot \frac{\mathbf{x}_i - \mathbf{x}_j}{r_{ij}} \cdot (\mathbf{v}_i - \mathbf{v}_j) \quad (4.32)$$

$$\frac{dW_{ij}^i}{dh_i} = -\frac{1}{h_i} \left( D_m W_{ij}^i + r_{ij} \frac{dW_{ij}^i}{dr_{ij}} \right) \quad (4.33)$$

$$\frac{d\rho_i}{dt} = \frac{1}{\beta_i} \sum_j^N m_j \nabla W_{ij}^i \cdot (\mathbf{v}_i - \mathbf{v}_j) + \sum_j^N \frac{dm_j}{dt} W_{ij}^i \quad (4.34)$$

where  $\beta_i = -\frac{1}{\rho_i D_m} \sum_j^N m_j r_{ij} \frac{dW_{ij}^i}{dr_{ij}}$ . Then, substituting Eq. (4.24) into Eq. (4.34), the SPH

approximation of the continuity equation is as follows.

$$\frac{d\rho_i}{dt} = \frac{1}{\beta_i} \sum_j^N m_j \nabla W_{ij}^i \cdot (\mathbf{v}_i - \mathbf{v}_j) + \rho_w \sum_j^N \frac{m_j}{\rho_j} R_j W_{ij}^i \quad (4.35)$$

As a result, we demonstrate that the use of the SPH summation operator for particle density (Eq. (4.17)) is related to a type of implicit discretization of the continuity equation (Vila, 1999).





#### 4.4 Discretization of the momentum equation

The Lagrangian variational approach shown in Eq. (4.36) is adopted to describe the motion of particles in shallow water flows (Rodriguez-Paz and Bonet, 2005):

$$\frac{d}{dt} \frac{\partial L}{\partial \mathbf{v}_i} - \frac{\partial L}{\partial \mathbf{x}_i} = 0 \quad i = 1, \dots, N \quad (4.36)$$

where  $L$  is the Lagrangian functional, which is expressed as  $L = K - \pi$ .  $K$  is the kinematic energy and  $\pi$  is the potential energy, which is the sum of the external energy ( $\pi_{\text{ext}}$ ) and the internal energy ( $\pi_{\text{int}}$ ).  $N$  is the total number of particles.

Substituting  $L = K - \pi$  into Eq. (4.36) and denoting the inertial, external and internal forces as  $\mathbf{I}_i$ ,  $\mathbf{F}_i$  and  $\mathbf{T}_i$ , respectively, we can obtain the following equations.

$$\mathbf{I}_i = \frac{d}{dt} \frac{\partial K}{\partial \mathbf{v}_i} - \frac{\partial K}{\partial \mathbf{x}_i}, \quad \mathbf{F}_i = -\frac{\partial \pi_{\text{ext}}}{\partial \mathbf{x}_i}, \quad \mathbf{T}_i = \frac{\partial \pi_{\text{int}}}{\partial \mathbf{x}_i} \quad (4.37)$$

$\mathbf{F}_i$  and  $\mathbf{T}_i$  can be calculated based on the following relationships:

$$\mathbf{F}_i = -m_i g \nabla b_i - \mathbf{S}_f \quad (4.38)$$

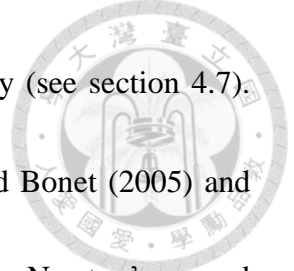
$$\mathbf{T}_i = \sum_j^N m_i m_j \left( \frac{p_j}{\beta_j \rho_j^2} \nabla_j W_{ji}^j - \frac{p_i}{\beta_i \rho_i^2} \nabla_i W_{ij}^i \right) \quad (4.39)$$

In the above, the pressure force  $p$  is calculated based on the hydrostatic law as

$$0.5 \rho_w g d_w^2.$$

After adding the stabilization term, Eq. (4.39) becomes

$$\mathbf{T}_i = \sum_j^N m_i m_j \frac{g}{2 \rho_w} \left[ \left( \frac{1}{\beta_j} + \Pi_{ij} \right) \nabla_j W_{ji}^j - \left( \frac{1}{\beta_i} + \Pi_{ij} \right) \nabla_i W_{ij}^i \right] \quad (4.40)$$



where  $\beta$  is the correction factor and  $\Pi_{ij}$  is the artificial viscosity (see section 4.7).

For details of the derivation, we refer readers to Rodriguez-Paz and Bonet (2005) and Ata and Soulaïmani (2005). Substituting Eqs. (4.37) and (4.40) into Newton's second law,  $\mathbf{I}_i = \mathbf{F}_i - \mathbf{T}_i$ , the particle acceleration  $\left(\frac{D\mathbf{v}}{Dt}\right)_i$  can be evaluated as follows:

$$\left(\frac{D\mathbf{v}}{Dt}\right)_i = -\mathbf{t}_i - g\nabla b_i - \mathbf{S}_{f,i} \quad (4.41)$$

where  $\mathbf{t}_i = \mathbf{T}_i / m_i$  (Vacondio *et al.*, 2012a).

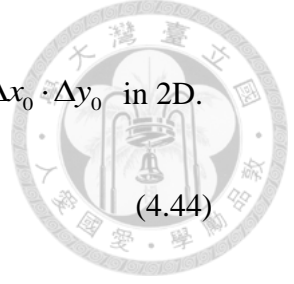
#### 4.5 Evolution of bed gradient term and friction term

Because of free motion of fluid particles, the elevation and the Manning coefficient roughness of each particle are both allowed to vary with particle location, and the interpolations of these two variables (Eq. (4.42) and Eq. (4.43)) are performed with the help of the bottom particles. The bottom particles are different from the fluid particles. They are also introduced at the beginning of the simulation, but are not controlled by governing equations. Moreover, they are fixed and distributed on a Cartesian uniform grid during the whole simulation (Vacondio *et al.*, 2011). Hence, the bottom elevation and the Manning coefficient roughness of fluid particle  $i$  can be calculated respectively by

$$b_i = \sum_{bp}^N V_{bp} b_{bp} \overline{W}_{ibp}^{bp} \quad (4.42)$$

$$n_i = \sum_{bp}^N V_{bp} n_{bp} \overline{W}_{ibp}^{bp} \quad (4.43)$$

where  $bp$  denotes the bottom particles,  $\overline{W}_{ibp}^{bp} = \overline{W}_{ibp}^{bp}(\mathbf{x}_i - \mathbf{x}_{j}^{bp}, h_{bp})$  denotes the corrected



kernel (Bonet and Lok, 1999), and  $V_{bp}$  is equal to  $\Delta x_0$  in 1D and  $\Delta x_0 \cdot \Delta y_0$  in 2D.

$$\bar{W}_{ibp}^{bp} = \frac{W_{ibp}^{bp}}{\sum_{bp}^N V_{bp} W_{ibp}^{bp}} \quad (4.44)$$

In addition, after calculating the bottom elevation for each fluid particle using Eq. (4.42),

the bottom elevation gradient of fluid particle  $i$  can be provided by using Eq. (4.45).

$$\nabla b_i = \sum_{bp}^N V_{bp} (b_{bp} - b_i) \tilde{\nabla}_i W_{ibp}^i \quad (4.45)$$

where  $\tilde{\nabla}_i W_{ibp}^i$  is the corrected gradient of kernel function (Bonet and Lok, 1999). Eq.

(4.45) can be also derived by substituting  $f = b$  into Eq. (3.20).

By means of a correction matrix  $\mathbf{L}$ , the corrected gradient of kernel function can be written as

$$\tilde{\nabla}_i W_{ibp}^i = \mathbf{L}_i \nabla W_{ibp}^i \quad (4.46)$$

where  $\mathbf{L}$  is calculated by

$$\mathbf{L}_i = \left[ \sum_{bp}^N \nabla W_{ibp}^i \otimes (\mathbf{x}_{bp} - \mathbf{x}_i) V_{bp} \right]^{-1}. \quad (4.47)$$

Actually there are three different ways for computing  $\nabla b$ :

1. Computing the bottom elevation of fluid particle ( $b_i$ ) by using the bottom particles,

then use the antisymmetric gradient formulation to computing  $\nabla b_i$ :

$$b_i = \sum_{bp}^N V_{bp} b_{bp} \bar{W}_{ibp}^{bp} \quad \text{for each fluid particle, then } (\nabla b)_i = \left[ \sum_j^N \frac{m_j}{\rho_j} (b_j - b_i) \nabla_i W_{ij}^i \right]$$

2. Directly computing  $\nabla b_i$  for each fluid particle by using the bottom particles:



$$\nabla b_i = \sum_{bp}^N V_{bp} b_{bp} \tilde{\nabla}_i W_{ibp}^{bp}$$

3. Computing the bottom elevation of fluid particle ( $b_i$ ) by using the bottom particles, then use the antisymmetric gradient formulation to computing  $\nabla b_i$  between the fluid particles and the bottom particles:

$$b_i = \sum_{bp}^N V_{bp} b_{bp} \overline{W}_{ibp}^{bp} \text{ for each fluid particle, then computing}$$

$$(\nabla b)_i = \left[ \sum_{bp}^N V_{bp} (b_{bp} - b_i) \nabla_i W_{ibp}^i (\mathbf{x}_i - \mathbf{x}_j^{bp}, h_i) \right].$$

The dam break event of the Toce river valley (Kao and Chang, 2012) is used as the test case for these three computing manners, but not any obvious differences between them were founded. In this thesis the 3<sup>rd</sup> manner is adopted.

#### 4.6 Velocity correction in momentum equation for mass variation and extreme small water depth

In the rainfall process (or infiltration), the calculated friction term becomes unstable due to very shallow water. Therefore, a correction (Eq. (4.48)) is adopted to evaluate the friction force term (Liang *et al.*, 2007; Costabile *et al.*, 2013):

$$\mathbf{v}_i^{n+1} = \frac{\mathbf{v}_i^*}{1 + \Delta t (\mathbf{S}_f / \mathbf{v})_i^n} \quad (4.48)$$

where  $\mathbf{v}_i^*$  is the velocity computed by Eq. (4.41), excluding the friction term.

Furthermore, as raindrops fall and become flowing fluid, the velocity of each fluid particle will change due to the conservation of momentum (Zhang and Cundy, 1989).



The corrected velocity of a fluid particle with varied mass is given by Eq. (4.49):

$$\underbrace{(m + \Delta m)}_{\text{particle mass after rainfall}} \mathbf{v}' = m\mathbf{v} \quad (4.49)$$

where  $\mathbf{v}'$  is the corrected velocity and  $\Delta m$  is the mass increase associated with raindrops or the mass decrease when infiltration occurs.

#### 4.7 Artificial viscosity and stabilization term

In hydrodynamic modeling, sometimes the simulation will generate unphysical numerical oscillation around the shock wave region. A shock wave is not a true physical discontinuity but a transition zone whose mean free paths is a few- molecules-long. To maintain the conservation law across the shock wave region needs to transform kinetic energy into heat energy. Such energy transformation can be treated as a kind of viscous dissipation in physical. Therefore, the inner force term of equation of motion is modified as follows:

$$\mathbf{T}_i = \sum_j^N m_i m_j \frac{g}{2\rho_w} \left[ \left( \frac{1}{\beta_j} + \Pi_{ij} \right) \nabla_j W_{ji}^j - \left( \frac{1}{\beta_i} + \Pi_{ij} \right) \nabla_i W_{ij}^i \right] \quad (4.50)$$

where  $\Pi_{ij}$  is the additional artificial viscosity in order to stabilize the numerical results.

There are two common choices of  $\Pi_{ij}$ . One is (Monaghan, 1989)

$$\Pi_{ij} = \begin{cases} \frac{-a\bar{c}_{ij}\phi_{ij} + b\bar{c}_{ij}\phi_{ij}^2}{\rho_{ij}} & \text{if } \mathbf{v}_{ij} \cdot \mathbf{x}_{ij} < 0 \\ 0 & \text{if } \mathbf{v}_{ij} \cdot \mathbf{x}_{ij} \geq 0 \end{cases} \quad (4.51)$$

and



$$\phi_{ij} = \frac{\bar{h}_{ij} \mathbf{v}_{ij} \cdot \mathbf{x}_{ij}}{|\mathbf{x}_{ij}|^2 + \eta^2} \quad (4.52)$$

where  $\bar{\xi}_{ij} = 0.5(\xi_i + \xi_j)$ ,  $\xi_{ij} = \xi_i - \xi_j$  which  $\xi$  can be any variables and  $\eta = 0.01\sqrt{\Delta x_0^2 + \Delta y_0^2}$  is a small constant for preventing denominator from becoming zero,  $c$  is the speed of infinitesimal perturbation, which can be sound or a water wave ( $=\sqrt{gd_w}$ ),  $a$  and  $b$  are constants which relate to the strength of the artificial viscosity, and usually set around 1.0.

Another method is modified from the Lax-Friedrichs flux (Ata and Soulaïmani, 2005), where the center flux is replaced by

$$\frac{1}{2}[F(x_i) + F(x_j)] + \Pi_{ij} \quad (4.53)$$

After some simplification processes,  $\Pi_{ij}$  is obtained as

$$\Pi_{ij} = -\frac{\bar{c}_{ij} \mathbf{v}_{ij} \cdot \mathbf{x}_{ij}}{\rho_{ij} \sqrt{|\mathbf{x}_{ij}|^2 + \eta^2}} \quad (4.54)$$

The advantage of the latter viscosity formula is that there needs no parameters to be tuned.

## 4.8 Time stepping and integration

Due to the symplectic nature of the leap-frog time integration scheme, it can conserve both the linear and angular momentums of a fluid particle. Thus, we use it to update the physical variables such as the position and velocity of a fluid particle, i.e., Eqs. (4.55) to (4.59).



$$\mathbf{v}_i^{n+1/2} = \mathbf{v}_i^{n-1/2} + \Delta t \left( \frac{D\mathbf{v}}{Dt} \right)_i^n \quad (4.55)$$

$$f_i^{n+1/2} = f_i^{n-1/2} + \Delta t \left( \frac{Df}{Dt} \right)_i^n \quad (4.56)$$

$$\mathbf{x}_i^{n+1} = \mathbf{x}_i^n + \Delta t \mathbf{v}_i^{n+1/2} \quad (4.57)$$

$$\mathbf{v}_i^{n+1} = \mathbf{v}_i^{n+1/2} + \frac{1}{2} \Delta t \left( \frac{D\mathbf{v}}{Dt} \right)_i^n \quad (4.58)$$

$$f_i^{n+1} = f_i^{n+1/2} + \frac{1}{2} \Delta t \left( \frac{Df}{Dt} \right)_i^n \quad (4.59)$$

In above equations,  $f$  denotes any other updated physical quantities such as  $\rho$  or pollution concentration  $C$ . In addition, because SPH is an explicit scheme, the time step is determined by satisfying the Courant-Friedrichs-Lewy (CFL) condition:

$$\Delta t = C_{CFL} \min_{i=1}^N \left( \frac{h_i}{\sqrt{gd_{w,i} + \|\mathbf{v}_i\|}} \right) \quad (4.60)$$

where  $C_{CFL}$  is the Courant number (0.4 in this study).

#### 4.9 Nearest neighboring particle searching (NNPS)

In SPH method, the smoothing kernel function of each particle has a compact support domain with a radius  $\kappa h$ . Only a finite number of particles are inside the support domain of the concerned particle, and involved in the concerned particle's weighting calculation. These particles are called the nearest neighboring particles of the concerned particle. The algorithm of how to search these particles will deeply affect the



computational efficiency. When particle number is too large, the search algorithm will cost the most computing resources. Two search algorithms are introduced here, all-pair search and link list.

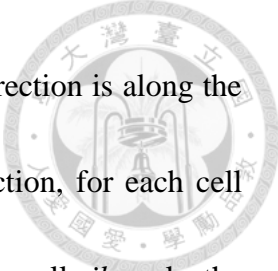
#### 4.9.1 All-pair search

All-pair search is the most direct particle search algorithm. For a given particle  $i$ , computing the distance  $\mathbf{x}_{ij}$  from  $i$  to any other particle  $j$ , and  $j$  runs from 1 to the total particle number  $N$ . If  $|\mathbf{x}_{ij}| \leq \kappa h_i$ , the  $j$ -th particle is determined to be within the support domain of the particle  $i$  with the smoothing length  $h_i$ . Thence  $j$  is referred as  $i$ 's nearest neighboring particle. However, if the smoothing length is not isometric, the particles will not belong to each other's nearest neighboring particles, and the Newton' third law of motion, the law about action and reaction forces, will not be satisfied. The complexity of the all-pair search is of order  $O(N^2)$ , where  $N$  is the total number of particles.

#### 4.9.2 Linked-list

In this search algorithm (Monaghan and Lattanzio, 1985), computational domain is divided in square cells with size  $2h$  ( $\kappa = 2$ ). For the concerned particle in the cell, only the particles in the neighboring cells will have the interactions. Thus, we just need to consider the particles in the neighboring cells and calculate the distances  $\mathbf{x}_{ij}$  between the concerned particle  $i$  and those neighboring particles.

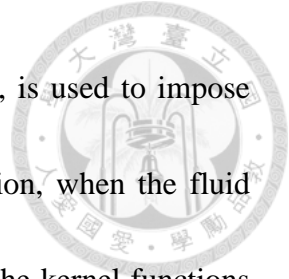




Take the 2D  $xy$ -plane domain for example, if the mainstream direction is along the  $y$ -direction, the code will sweep through the cells along the  $y$ -direction, for each cell along  $x$ -direction. To avoid repeating the calculation, for the center cell,  $ik$ , only the neighboring cells of N, NE, E and SE are involved in the neighboring search calculation. The rest of the four cells were already considered through the previous sweepings. In 1D domain, it is much easier because we just calculate only two cells in a step, the center cell  $ik$ , and the next downstream cell. In 3D, 13 out 26 neighboring cells are considered in a single sweeping. They are 4 cells in  $n$ th layer and 9 cells in the next layer. In Fig. 4.4, the possible neighbors of the fluid particles are in the adjacent cells. The neighboring fluid particles which have the practical interactions with the concerned particle are marked by black dots in the circular. In Fig. 4.5, the mainstream direction is at the  $y$  direction, so the sweeping direction goes from left to right and then from down to up. For example, first choose a certain  $y$ -th column, the code runs from the bottom cell to the top cell of the column. Thereafter, the code moves to the next right column and repeats the step.

#### **4.10 Wall boundary conditions**

Wall boundary conditions are used to maintain the well-defined properties of dynamics system with the governing equations. There are many kinds of wall boundary condition treatments in the literatures, but only some of them are introduced here.



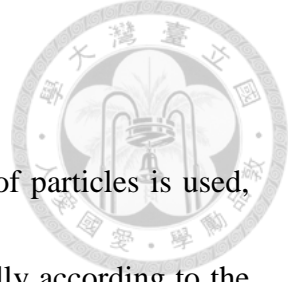
Another type of particle, usually called the solid boundary particle, is used to impose the boundary conditions and to confine the flow domain. In addition, when the fluid particles flow near the boundaries, the compact support domain of the kernel functions will be truncated. Thus, some treatments should be taken on those particles to reduce the errors associated with the application of wall boundary conditions.

#### 4.10.1 The Ghost particles method

In this method, the solid boundary particles aren't controlled by governing equations. They do not move but fixed at the original positions during the whole simulation. In addition, they impose an external force on fluid particles, preventing them from flowing across the boundary. However, the fluid particles have no effects on the solid boundary particles. The repulsive boundary force is exerted analog to the molecular force of Lennard-Jones form:

$$PB_{ij} = \begin{cases} D \left[ \left( \frac{x_0}{|\mathbf{x}_{ij}|} \right)^{n_1} - \left( \frac{x_0}{|\mathbf{x}_{ij}|} \right)^{n_2} \right] \frac{\mathbf{x}_{ij}}{|\mathbf{x}_{ij}|^2} & \left( \frac{x_0}{|\mathbf{x}_{ij}|} \right) \leq 1 \\ 0 & \left( \frac{x_0}{|\mathbf{x}_{ij}|} \right) > 1 \end{cases} \quad (4.61)$$

where the constant  $n_1$  and  $n_2$  are usually taken as 12 and 4, respectively. The value of  $D$  is depended cases by cases and is taken in the same scale with the square of the maximum velocity of particles.  $x_0$  is usually chosen close to the initial particle spacing. Note that the spacing of boundary particles is usually half of the initial fluid particles



spacing so that the simulation can get the better simulation results.

Furthermore, to complement the support domain, a new kind of particles is used, called the ghost particles. These particles are generated symmetrically according to the corresponding fluid particles in each step, and involved in the neighbor particle searching algorithm and kernel function calculation. Similarly, the parameters of the ghost particles are also not evolved during the simulation, just like the solid boundary particles. In Fig. 4.6, the ghost particles are set at least four columns at the boundary to reduce the truncation effect of the kernel function.

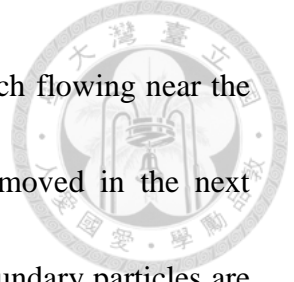
#### 4.10.2 The simplified MVBP method

The modified virtual boundary particle (MVBP) method is introduced by (Vacondio *et al.*, 2012b). This method is a simplified from MVBP. Like MVBP method, for a given fluid particle, two fictitious particles are generated related to a certain wall boundary particle by using the local point-symmetry. If the distance between the fluid particle and the wall boundary particle is less than  $2h$ , two fictitious particles will be located at

$$\mathbf{x}_{f,1} = 2\mathbf{x}_b - \mathbf{x}_i \quad (4.62)$$

$$\mathbf{x}_{f,2} = 4\mathbf{x}_b - \mathbf{x}_i \quad (4.63)$$

where  $\mathbf{x}_f$ ,  $\mathbf{x}_b$  and  $\mathbf{x}_i$  are the positions of fictitious particles, wall boundary particles and inner fluid particles, respectively. In Fig. 4.7, fictitious particles are used just for



interpolating the physical quantities of the inner fluid particles, which flowing near the wall boundary, and thereafter these fictitious particles will be removed in the next computing step. Furthermore, in this method two additional wall boundary particles are added on the corner when internal angles of the corner is small than or equal to 180 degrees ( $\leq 180^\circ$ ) for reducing the kernel truncation effect. Similarly, the wall boundary particles still work as a role which imposes the boundary forces on the inner fluid particles. And the formulation of the boundary force used in this method was introduced by Monaghan *et al.* (2004). By this formulation, the forces acting on the boundary particles can also be calculated, or even used to simulate the floating objects. The force per unit mass on fluid particle  $i$  due to boundary particle  $k$  is

$$\mathbf{f}_{ik} = \frac{m_k}{m_i + m_k} B(x, y) \mathbf{n}_k \quad (4.64)$$

where  $B(x, y)$  is a function to be chosen,  $\mathbf{n}_k$  is the unit normal vector from the fluid particle to the boundary. The total boundary force per unit mass on fluid  $i$  is  $f_i = \sum_k f_{ik}$ .

Moreover, according to the action-reaction forces of Newton's third law of motion,

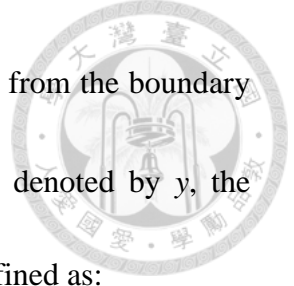
$m_k \mathbf{f}_{ki} = -m_i \mathbf{f}_{ik}$ , the forces acting on the solid boundary particle  $k$  can be evaluated as:

$$\mathbf{f}_{ik} = -\frac{m_i}{m_i + m_k} B(x, y) \mathbf{n}_k \quad (4.65)$$

And the total force per unit mass on boundary particle  $k$  due to all fluid particles is

$f_k = \sum_i f_{ki}$ . The equation of motion of fluid particle  $i$  becomes

$$\left( \frac{D\mathbf{v}}{Dt} \right)_i = -\mathbf{t}_i - g \nabla b_i - \mathbf{S}_{f,i} + \mathbf{f}_i \quad (4.66)$$



$B(x, y)$  is written as a product  $\Gamma(y)\chi(x)$ . The distance is measured from the boundary particle to fluid particle, and the connection (normal) direction is denoted by  $y$ , the vertical (tangential) direction is denoted by  $x$ . Therefore  $\chi(x)$  is defined as:

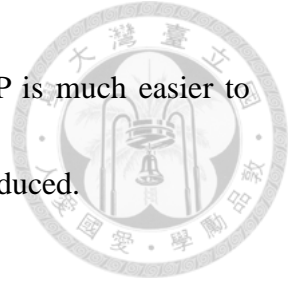
$$\chi(x) = \begin{cases} \left(1 - \frac{|x_{ik}|}{\Delta x_b}\right) & \text{if } 0 < |x_{ik}| < \Delta x_b, \\ 0 & \text{otherwise,} \end{cases} \quad (4.67)$$

where  $\Delta x_b$  is the wall boundary particle spacing,  $x_{ik}$  means the tangential distance between the wall boundary particle and the fluid particle. The function  $\chi(x)$  can ensure that a fluid particle moving parallel to the wall boundary will feel the same boundary force.  $\Gamma(y)$  is defined by

$$\Gamma(y) = \beta \begin{cases} \frac{2}{3} & \text{if } 0 < q \leq \frac{2}{3}, \\ (2q - \frac{3}{2}q^2) & \text{if } \frac{2}{3} < q \leq 1, \\ \frac{1}{2}(2 - q)^2 & \text{if } 1 < q \leq 2, \\ 0 & \text{otherwise,} \end{cases} \quad (4.68)$$

where  $\beta = 0.02c_s^2 / |y_{ik}|$ ,  $q = |y_{ik}|/h$  and  $y_{ik}$  denotes the normal distance between the wall boundary particle and the fluid particle.  $\beta$  estimates the maximum force per mass used to stop the particle moving with the maximum speed, and  $1/y_{ik}$  can ensure to prevent a faster moving particle from penetrating the walls.

Generally, ghost particles give fewer disturbances to the flow field. However, when



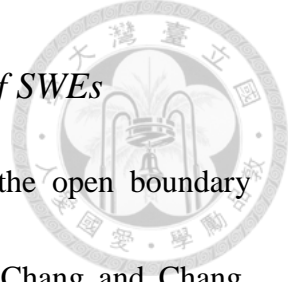
dealing with complicated domain geometries, the simplified MVBP is much easier to use, although a few non-physical pressure oscillations might be introduced.

#### 4.10.3 Periodic boundary condition

By applying periodic boundary condition, fluid particles near the lateral boundary will interact with particles at the complementary lateral boundary on other side of the domain. Namely, the influence support domain of particle  $i$  will be extended to the complementary boundary side continuously. In Fig. 4.8, the support domain of the particle  $i$  is extended beyond the top lateral boundary and continued through the periodic boundary at the bottom of the figure.

### 4.11 Open boundary conditions

It is more intuitive by using the open boundary conditions when dealing with problems on some landscapes, like the river or channel. Another advantage is that the open boundary can be used to limit the computational domain to our interest; thence it saves the memories and computing time. However, in meshfree methods, it is not straightforward to apply the open boundary conditions as traditional grid-based methods. In SPH scheme with open boundary conditions, particles will be inserted in and removed from the computational domain. But it should avoid making perturbations on the inner fluid when inserting particles (Federico *et al.*, 2012). Two methods for the open boundary are introduced below.



#### 4.11.1 Method of specified time interval for 1D Q-A form of SWEs

Method of specified time interval can be used to evaluate the open boundary conditions for 1D SWEs with any channel cross-sectional areas (Chang and Chang, 2013). Fig. 4.9 illustrates the method of specified time interval. The characteristic equations are discretized by the finite difference approximations as following:

$$C^+ : u_S = u_R - \frac{g}{c_R}(d_{w,S} - d_{w,R}) + g(S_{0,R} - S_{f,R})\Delta t \quad (4.69)$$

$$C^+ : \frac{x_S - x_R}{\Delta t} = u_R + c_R \quad (4.70)$$

$$C^- : u_P = u_L - \frac{g}{c_L}(d_{w,P} - d_{w,L}) + g(S_{0,L} - S_{f,L})\Delta t \quad (4.71)$$

$$C^- : \frac{x_P - x_L}{\Delta t} = u_L + c_L \quad (4.72)$$

In addition, the linear interpolation relationship among points C, D and R in Fig. 4.9 are

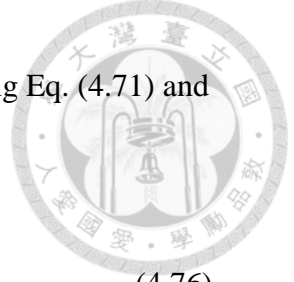
$$\frac{u_D - u_R}{u_D - u_C} = \frac{x_S + x_R}{\Delta x_0} = \frac{(u_R + c_R)\Delta t}{\Delta x_0} \quad (4.73)$$

$$\frac{c_D - c_R}{c_D - c_C} = \frac{(u_R + c_R)\Delta t}{\Delta x_0} \quad (4.47)$$

$$\frac{d_{w,D} - d_{w,R}}{d_{w,D} - d_{w,C}} = \frac{(u_R + c_R)\Delta t}{\Delta x_0} \quad (4.75)$$

With above Eqs. (4.69)-(4.75), we can know the velocities and water depths at the in/outflow boundaries (e.g. points P, L, R, and S in Fig. 4.9). Afterwards, the open boundary conditions are solved according to the local Froude number at the in/outflow boundaries:

1.a subcritical inflow condition: the water discharge is prescribed and the water depth



is calculated through Eq. (4.77) which is derived from combining Eq. (4.71) and

Eq. (4.76):

$$Q_p = A_p u_p \quad (4.76)$$

$$Q_p = A_p \left[ u_L + \frac{g}{c_L} (d_{w,p} - d_{w,L}) + g (S_{0,L} - S_{f,L}) \Delta t \right] \quad (4.77)$$

1.b subcritical outflow condition: the water depth is prescribed and the water discharge

is determined by using Eq. (4.79) which is derived from combining Eq. (4.69) and

Eq. (4.78):

$$Q_S = A_S u_S \quad (4.78)$$

$$Q_S = A_S \left[ u_R + \frac{g}{c_R} (d_{w,S} - d_{w,R}) + g (S_{0,R} - S_{f,R}) \Delta t \right] \quad (4.79)$$

2.a supercritical inflow condition:

$$\text{Both } Q_p \text{ and } d_{w,p} \text{ are prescribed.} \quad (4.65)$$

2.b supercritical outflow condition: there is not necessary to specify the boundary

conditions there.

The setup of inflow zone and outflow zone is the same with 2D domain (see section 4.9.2

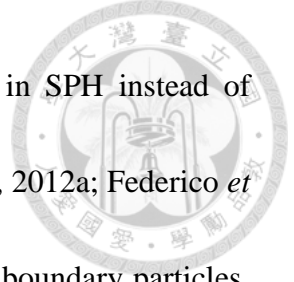
and Fig. 4.10).

#### 4.11.2 Riemann invariants for 2D $u$ - $d_w$ form of SWEs

In 2D open boundary problems since there are infinite characteristic curves, it is

difficult to determine the suitable one to be used. Thus to date only the Riemann





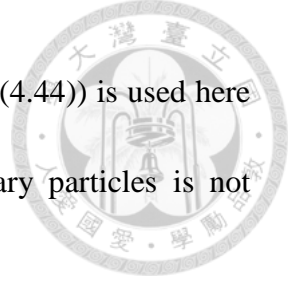
invariants can be used to solve the 2D open boundary problems in SPH instead of solving the discretization of characteristic equations (Vacondio *et al.*, 2012a; Federico *et al.*, 2012). In Fig. 4.10, there are two buffer zones filled with open boundary particles.

One is the inflow zone located at the upstream of the fluid domain, and the other one is at the outflow zone of the downstream. Open boundary particles are added to update the acceleration and the water depth of the fluid particles as well as apply the boundary conditions. Each buffer zone is at least  $2h$  long and will be placed 4 rows of open boundary particles for complementing the kernel support of fluid particles near the buffer zone. At the inflow zone, the inflow particle which flows across the inflow threshold and exits from the inflow region will become a fluid particle. At the same time, a new inflow particle is created and inserted into the inflow zone. Similarly, a fluid particle which crosses the outflow threshold will become an outflow particle. When the outflow particles cross the outlet, they will be removed from computing domain. These removed particles can be deleted or stored for reuse. The water depths and velocities of the open boundary particles are assigned or updated according to the characteristic boundary method with the extrapolation formula as follows (Vacondio, 2010):

$$\mathbf{v}_i^o = \sum_j \mathbf{v}_j^f \bar{W}_i(\mathbf{x}_i^o - \mathbf{x}_j^f, h^o) V_j^f \quad (4.61)$$

$$d_i^o = \sum_j \bar{W}_i(\mathbf{x}_i^o - \mathbf{x}_j^f, h^o) V_j^f \quad (4.62)$$

where the superscript  $o$  indicates the in/outflow particles and the superscript  $f$  denotes



the fluid particles. The kernel  $\overline{W}_i$  corrected by Shepard filter (Eq. (4.44)) is used here since that the support domain of kernel function of open boundary particles is not complete.

The open boundary conditions are imposed on these two buffer zones according to the characteristic method with Riemann invariants ( $v \pm 2c$ ) (Toro, 1997) and the local Froude number as follows:

1.a subcritical inflow condition:

$$d_b = \left[ \frac{1}{2\sqrt{g}}(v_{i,n} - v_{b,n}) + \sqrt{d^o} \right]^2, \quad \mathbf{v}_b \text{ is imposed.} \quad (4.63)$$

where,  $v_{b,n}$  and  $d_b$  are the normal velocity and the water depth calculated at the boundary, and  $v_{i,n}$  is the normal velocity of the inner fluid particles.

1.b subcritical outflow condition:

$$v_{b,n} = v_n^o + 2\sqrt{g}(\sqrt{d^o} - \sqrt{d_b}), \quad d_b \text{ is imposed.} \quad (4.64)$$

2.a supercritical inflow condition:

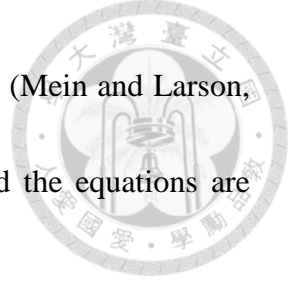
$$\text{Both } \mathbf{v}_b \text{ and } d_b \text{ are imposed.} \quad (4.65)$$

2.b supercritical outflow condition:

$$v_{b,n} = v_n^o, \quad d_b = d_n^o \quad (4.72)$$

## 4.12 Green-Ampt Infiltration module

The infiltration simulation is one of the phenomena that cause the mass reduction



from the runoff flows. In this thesis, the revised Green-Ampt model (Mein and Larson, 1973; Fiedler and Ramirez, 2000; Liu *et al.*, 2004) is adopted and the equations are written as:

$$f = \frac{dF}{dt} = K_s \left[ 1 + \frac{\Delta\theta \cdot \Psi}{F} \right] \quad (4.73)$$

$$F = K_s t + S_u \Delta\theta \ln \left[ 1 + \frac{F}{\Psi \Delta\theta} \right] \quad (4.74)$$

where  $F$  is the cumulative infiltration capacity,  $f$  is the infiltration rate,  $K_s$  is the saturated hydraulic conductivity of the soil (or the infiltration coefficient, it can be the function of space, e.g.  $K_s = K_s(x, y)$  (Woolhiser *et al.*, 1996)),  $\Delta\theta = \theta_s - \theta_i$ , and  $\theta_s$  is the saturated volumetric water content,  $\theta_i$  is the initial volumetric water content, and  $\Psi$  is the soil suction at the wetting front.

Water will pond on the surface at the moment when the rainfall intensity starts to be greater than the infiltration rate. Thus ponding time  $t_p$  represents the time between the starting of the rainfall and the time at which ponding occurs on the ground surface. At ponding time  $t_p$ , the present cumulative infiltration  $F_p$  can be calculated with Eq. (4.73) by substituting the infiltration equal to the rainfall intensity,  $f = R$

$$F_p = \frac{\Psi \Delta\theta}{R / K_s - 1} \quad (4.75)$$

So the ponding time can be calculated by

$$t_p = F_p / R \quad (4.76)$$

The equivalent time origin for potential infiltration after ponding is



$$t_0 = t_p - \frac{1}{K_s} \left( F_p - \Psi \Delta \theta \ln \left[ 1 + \frac{F_p}{\Psi \Delta \theta} \right] \right) \quad (4.77)$$

The real infiltration is obtained by translating the curve back to the right by  $t_0$  (Liu *et al.*, 2004). The infiltration capacity  $F$  at the next step is computed by solving the iteration of Eq. (4.74)

$$F^{n+1} - F^n - \Psi \ln \left[ \frac{F^{n+1} + \Psi \Delta \theta}{F^n + \Psi \Delta \theta} \right] = K_s \Delta t \quad (4.78)$$

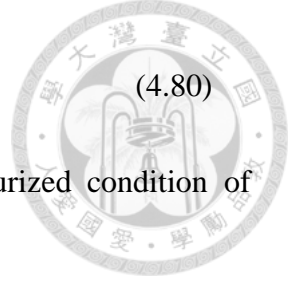
Eq. (4.78) is valid even for the variable saturated hydraulic conductivity  $K_s$ . At the end  $f^{n+1}$  is determined by using Eq. (4.73).

#### 4.13 1D SPH sewer module

Herein we develop a SPH sewer module for simulating the storm sewers based on two-component approach (TPA) (Vasconcelos *et al.*, 2006b; Vasconcelos and Weight, 2007; Sanders and Bradford, 2011). TPA assumes that the unsteady pressurized flow is compressible and an elastic behavior for the pipe walls and it is a framework describing the flow regime transition that decouples the hydrostatic pressure from surcharged pressures occurring only in pressurized conditions. Thus TPA can solve the coupling free surface and pressurized flows in pipes by only using SWEs and the addition of the surcharge head term. The 1D Lagrangian  $Q$ - $A$  form of SWEs associated with TPA for prismatic conduits such as pipe is given by:

$$\frac{DA}{Dt} = -A \frac{\partial}{\partial x} \left( \frac{Q}{A} \right) + (R - f) \quad (4.79)$$

$$\frac{DQ}{Dt} = -Q \frac{\partial}{\partial x} \left( \frac{Q}{A} \right) - gA \frac{\partial}{\partial x} (d_w + d_s) + gA(S_0 - S_f) \quad (4.80)$$



where  $d_s$  is the pressure head when the pipe is under the pressurized condition of full-pipe flow and computed by

$$d_s = \frac{a^2}{g} \frac{\Delta A}{A_{pipe}} \quad (4.81)$$

where  $a$  is the acoustic wave-speed and  $\Delta A = A - A_{pipe}$  represents the difference between the flow cross-sectional area and the pipe cross-sectional area. The SPH discretization of Eq. (4.80) for particle  $i$  is

$$\begin{aligned} \frac{DQ_i}{Dt} = & -\frac{Q_i}{A_i} \sum_j m_j \left( \frac{Q_j}{A_j} - \frac{Q_i}{A_i} \right) \overline{\nabla W}_i \\ & - gA_i^2 \sum_j m_j \left( \frac{d_{w,i} + d_{s,i}}{A_i^2} + \frac{d_{w,j} + d_{s,j}}{A_j^2} \right) \overline{\nabla W}_i + gA_i (S_{0,i} - S_{f,i}) \end{aligned} \quad (4.82)$$

The algorithm for computing  $d_s$  is as follows (Vasconcelos *et al.*, 2006a).

1. free surface flow: if no transition occurs,  $d_w$  is a function of cross sectional area and  $d_s$  is zero throughout the computational domain
2. free surface flow  $\rightarrow$  surcharge flow:  $d_w$  is equal to pipe diameter and  $d_s$  becomes positive at that location and computed by Eq. (4.81) (pressurization)
3. surcharge flow  $\rightarrow$  not surcharge flow:
  - a. with ventilation: free surface flow is regenerated ( $d_w = d_w(A)$ ,  $d_s = 0$ ).
  - b. without ventilation: low pressure transient wave is generated,  $d_w$  is kept at the value of pipe diameter and  $d_s$  becomes negative.



Besides, two binary parameters are needed to record the three states for each particle (free surface flow, pressure flow, depression flow): *sur* (surcharge) and *vent* (ventilation):

1. *sur* = 1 if surcharge, else *sur* = 0.
2. *vent* = 0 if with ventilation, else *vent* = 1.

Thus, for each particle when the state is

- a. free surface flow: *sur* = 0 and *vent* = 0
- b. pressure flow: *sur* = 1
- c. depression flow: *sur* = 0 and *vent* = 1

The surcharge state of a fluid particle is decided by the comparison between the flow cross sectional area and the pipe cross sectional area:

$$A_i \geq A_{pipe} \rightarrow sur = 1 \text{ else } sur = 0 \quad (4.83)$$

The ventilation state of a fluid particle *i* is decided by its two neighbor particles, *i-1* and *i+1* in 1D situation such as (multiplicative relationship)

$$vent_i^{n+1} = vent_{i-1}^n \cdot vent_i^n \cdot vent_{i+1}^n \quad (4.84)$$

We use *vent* = 0 with ventilation because the state of ventilation should be able to transfer. For example, if a fluid particle with undecided state is next to a fluid particle with ventilation, it will become ventilation state. Or if a fluid particle without ventilation (*vent* = 1) contacts with a fluid particle with ventilation (*vent* = 0), then it

will become ventilation state too in next step due to Eq. (4.84) (even if this particle contacts the non-ventilation particle at the same time).



#### **4.14 Calculation process**

The calculation process of SPH-SWEs is illustrated in Fig. 4.11. After inputting initial conditions from data files, boundary particles are generated according to the imposed boundary conditions. Next the code will execute the nearest neighbor particle searching and calculate the smoothing kernel function. Afterwards, calculation of density and force terms are carried out for the governing equations. At the end, the physical quantities are updated by integrating the governing equations, and if the smoothing length is variable, it is also updated before entering the next loop. The flow charts circled by the dotted line are included in the main loop, and it will repeat until the program computation is finished.

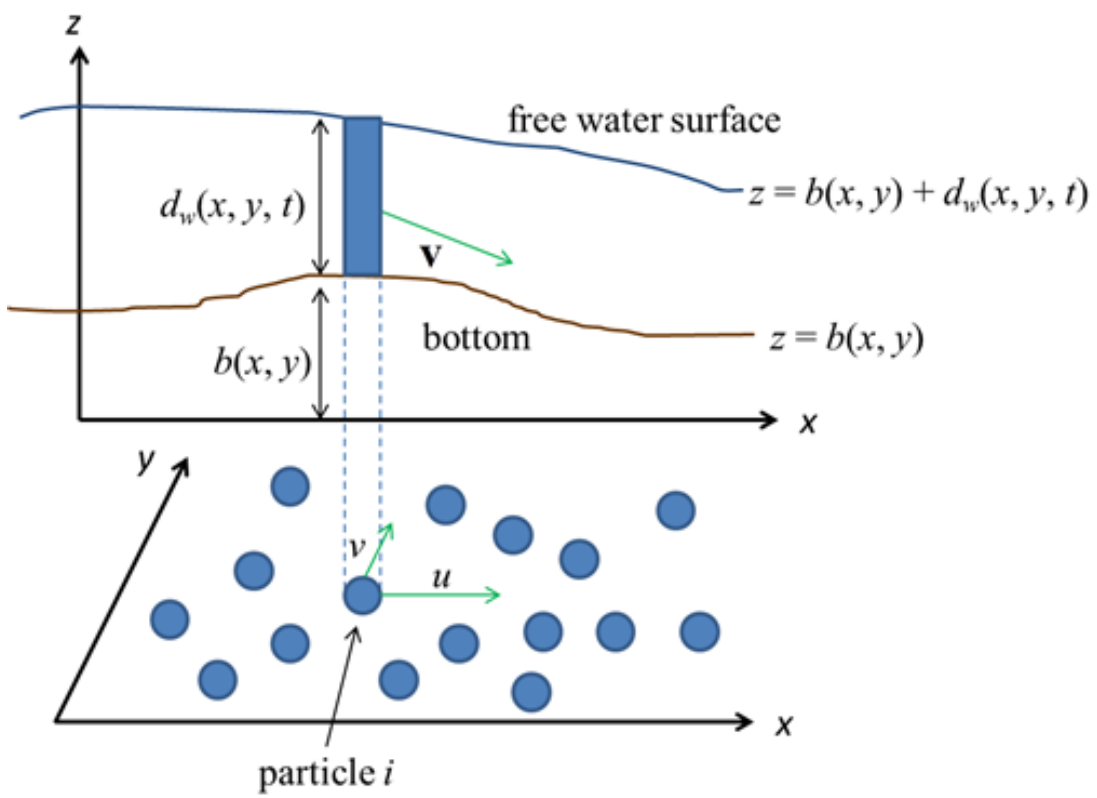


Fig. 4.1 Definition sketch of SPH with shallow water equations



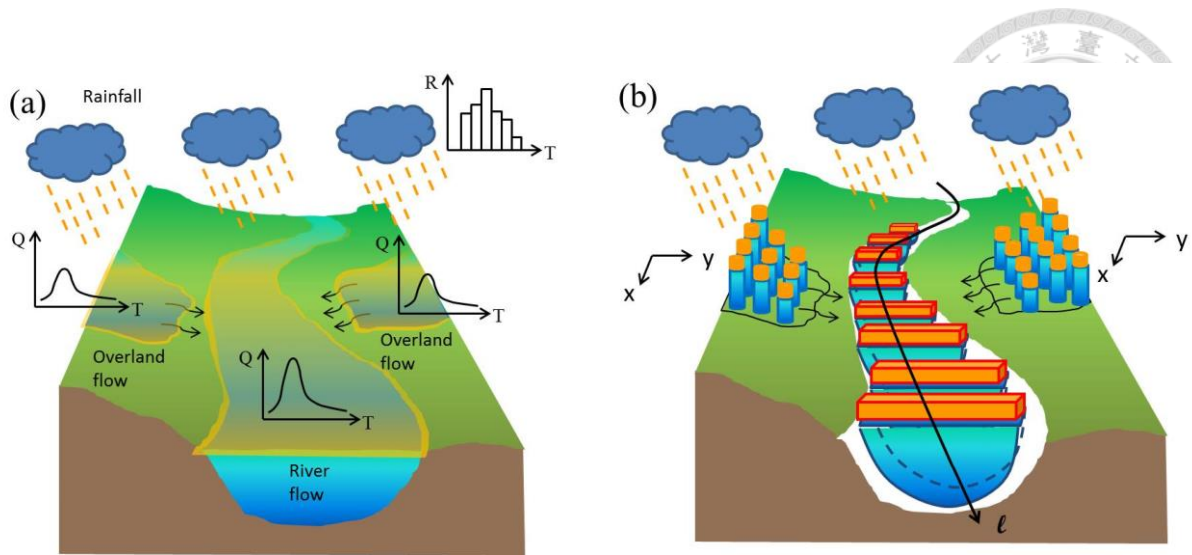


Fig. 4.2 (a) Hydrologic phenomena of rainfall, overland flows and river flows and (b) SPH-SWE modeling of hydrologic phenomena.

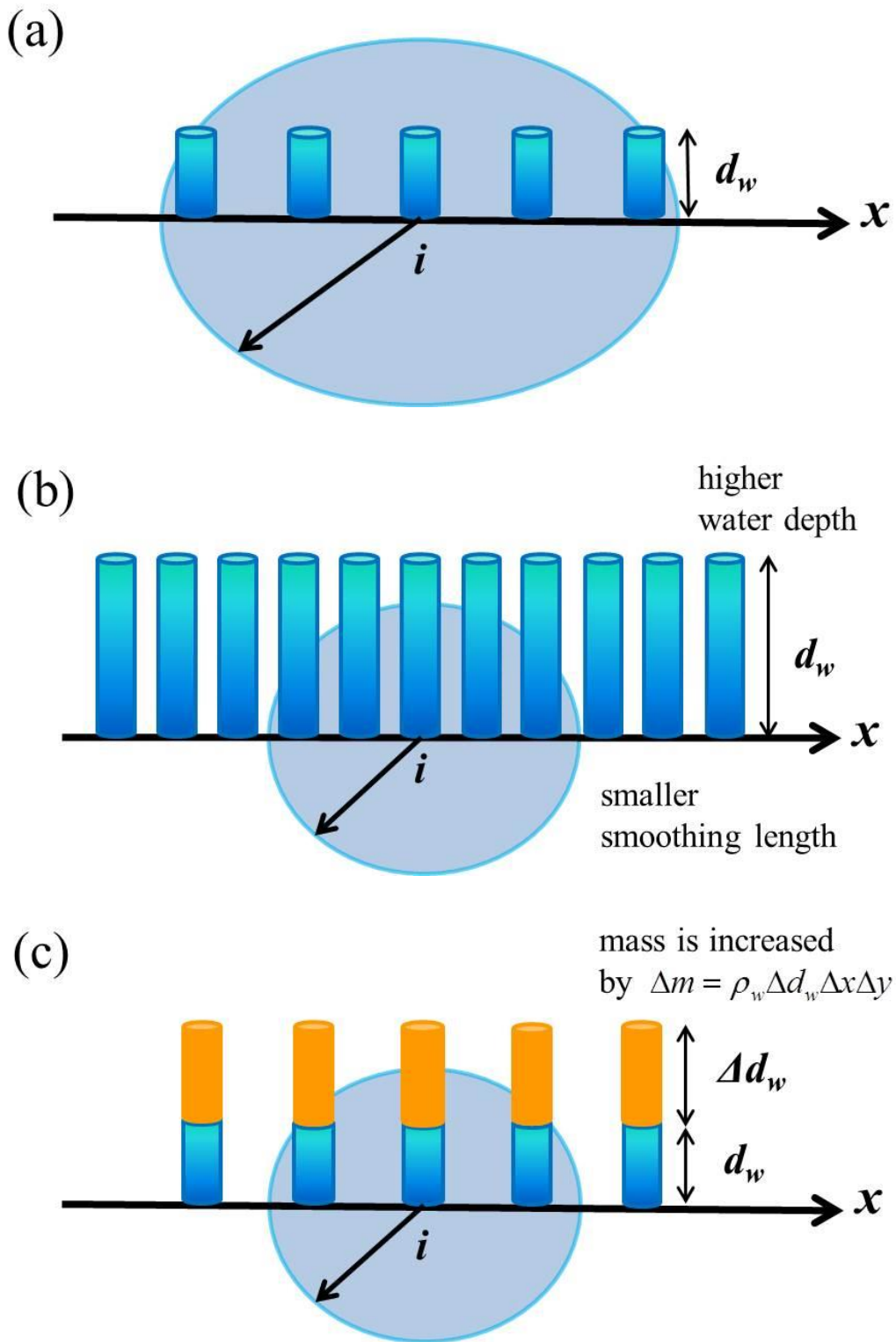


Fig. 4.3 Variations in the smoothing length of a fluid particle with different water depths, (a) the smoothing length  $h$  and water depth  $d_w$ , (b) a smoothing length of  $0.5 h$  and a water depth of  $2 d_w$  and (c) a smoothing length of  $0.5 h$ , water depth of  $d_w$  and additional water depth  $\Delta d_w$  caused by rainfall.

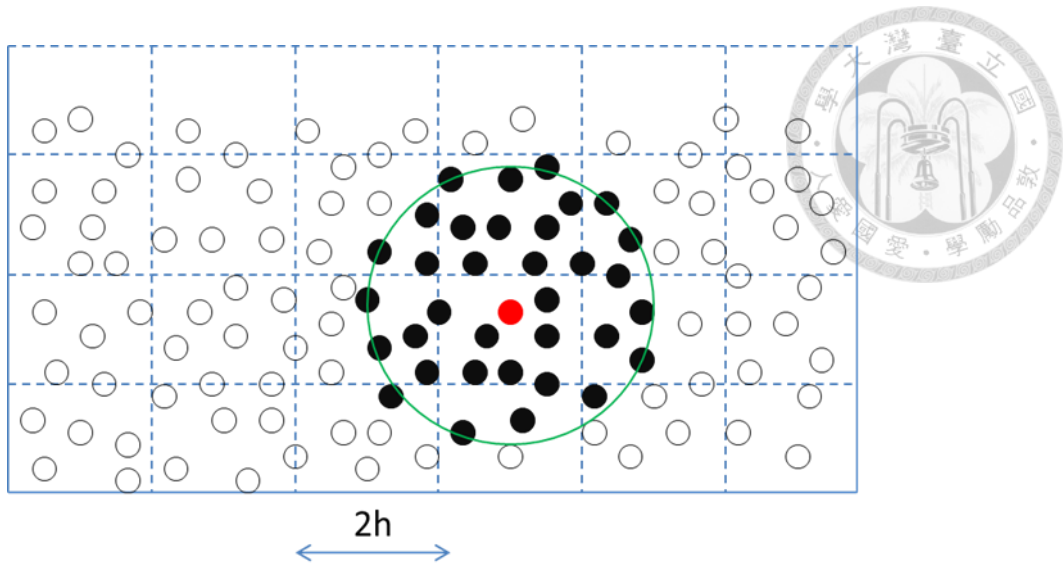


Fig. 4.4 Linked-list and neighbor particles (SPHysics).

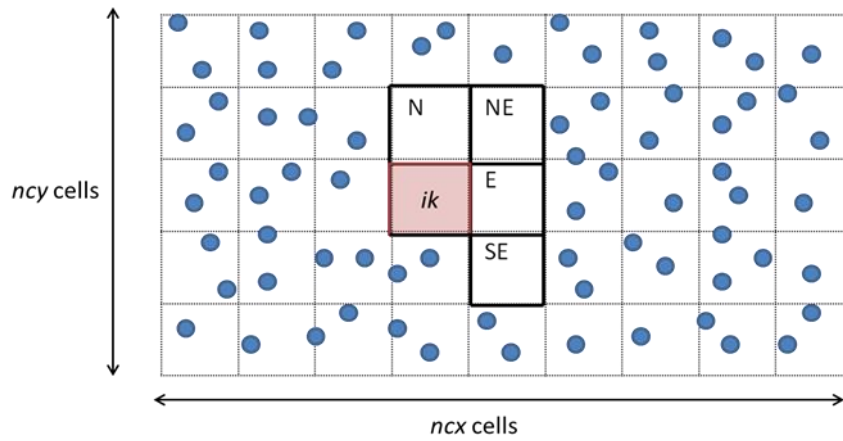


Fig. 4.5 Sweeping through grid cells in 2D domain (SPHysics).

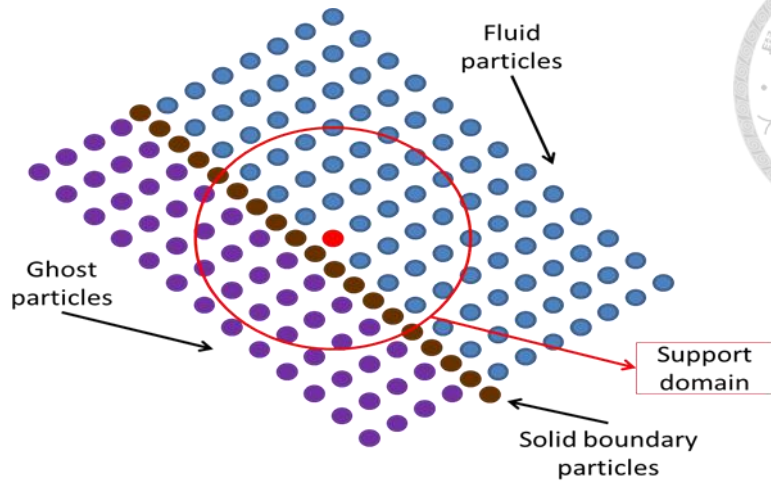


Fig. 4.6 Illustration of the ghost particle method.

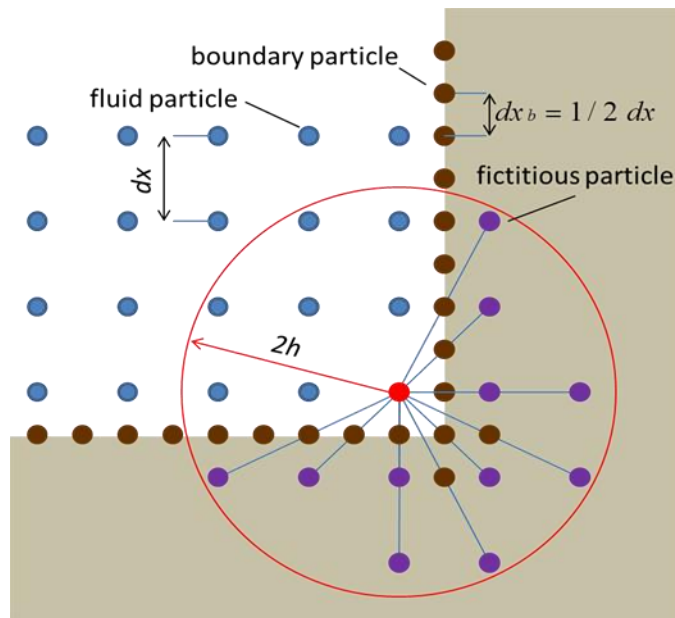


Fig. 4.7 Illustration of the MVBP method (Vacondio *et al.*, 2012b).

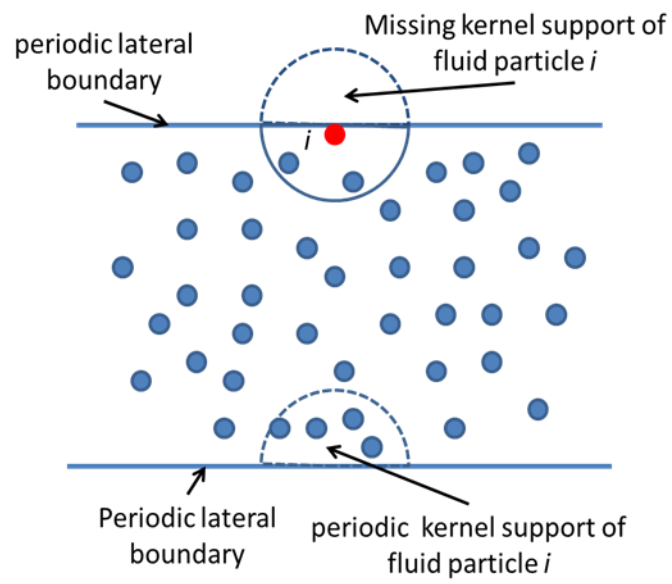


Fig. 4.8 Illustration of periodic boundary: lateral periodic boundaries (SPHysics).

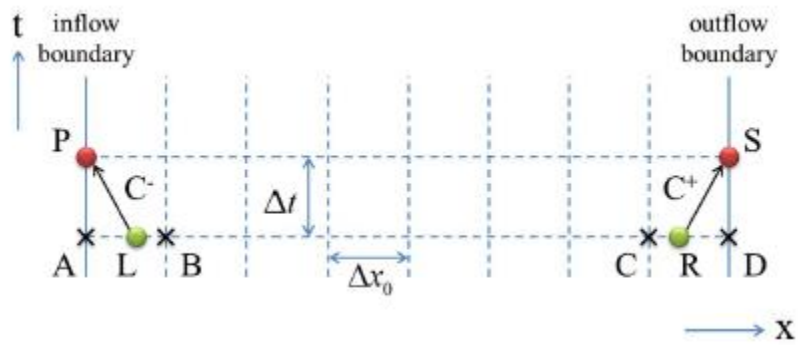


Fig. 4.9 Sketch of the method of specified time interval (Chang and Chang, 2013)

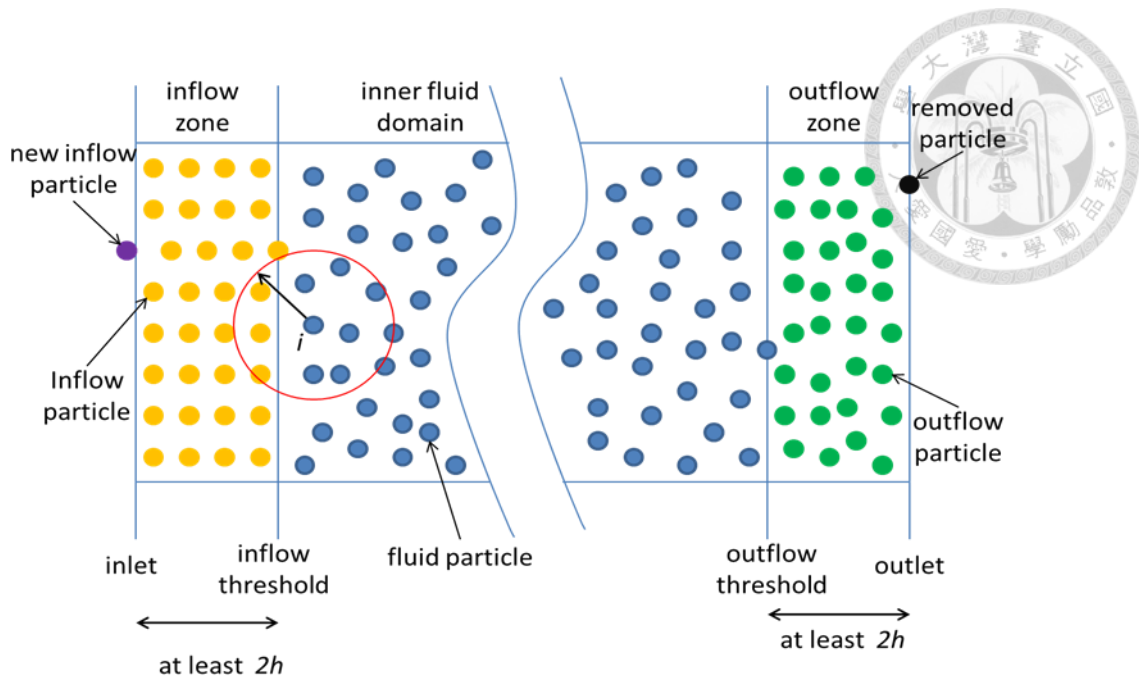


Fig. 4.10 Illustration of open boundary condition: inflow zone and outflow zone.

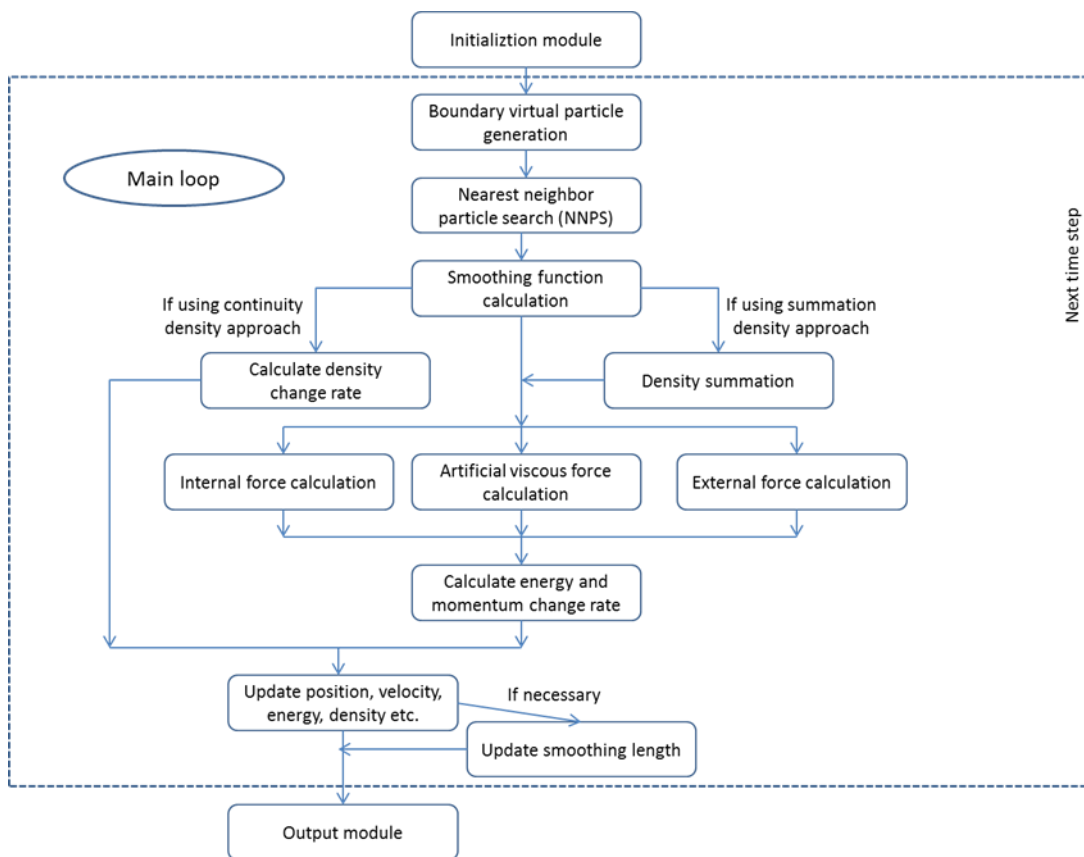


Fig. 4.11 The calculation flow chart (Liu and Liu, 2003).

## Chapter 5 Model validations and applications



In this section, the new treatment of using mass-varied particles in the SPH-SWE is examined based on three benchmark cases and two applications including uniform rainfall over a 1D flat channel, nonuniform rainfall over a 1D three-slope channel, uniform rainfall over a 2D experimental plot, Green-Ampt infiltration and 1D pipe flow with a hydraulic jump. The convergence of the particle number is explored for the first and third cases because the steady simulated results are given in these two cases. In addition, we investigate the accuracy of the simulated results compared to the exact solutions, the measured data and the simulated solutions resulting from mesh-based numerical models. It should be emphasized that a remeshing procedure proposed by Chaniotis *et al.* (2002) is performed at each step in the first four cases to provide the physical information regarding the particles on a dry bed. Following the remeshing procedure, the positions of the fluid particles are reinitialized on a uniform grid at the end of each step. Then, the physical quantities of the reinitialized fluid particles are updated via Eq. (3.11). All of the numerical simulations are performed using an Intel(R) Core(TM) i7-2600 CPU 3.4 GHz PC equipped with 4GB RAM.

To investigate the convergence and numerical accuracy of the proposed treatment, the relative  $L_2$  norm error based on the velocity is calculated as follows:

$$L_2 = \sqrt{\frac{\sum_{i=1}^N (u_i - u_i^{\text{ref}})^2}{\sum_{i=1}^N (u_i^{\text{ref}})^2}} \quad (5.1)$$



where  $N$  is the number of uniform grids or measured points and the superscript ref denotes the reference solution obtained from exact solutions, measured data, SPH-SWE simulated solutions at the highest spatial resolution, or mesh-based simulation solutions.

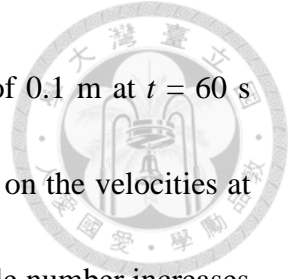
## 5.1 Uniform rainfall over a 1D flat channel

The first case study is uniform rainfall over a 1D 4 m-long flat channel with a slope of 0.05 (Delestre *et al.*, 2009). The total simulation time is 250 s. A rainfall duration from  $t = 5$  s to  $t = 125$  s is defined for rainfall with a constant intensity of 50 mm/h. This rainfall is converted to runoff within the region of 0 to 3.95 m in the channel. Initially, the water depth of each fluid particle is set to be an extremely small water depth of  $10^{-4}$  cm. A fixed wall is established at the upstream boundary, and a free outflow boundary condition is imposed downstream. A Darcy friction factor of 0.15 is adopted to compute the friction force on a fluid particle.

### 5.1.1 Convergence analysis of the particle number

Particle numbers of 50, 100, 200, 400 and 800 (i.e., the initial particle spacings  $\Delta x_0$  are 0.08, 0.04, 0.02, 0.01 and 0.005 m, respectively) in the computational domain are considered. The reference velocities are obtained by the proposed SPH-SWE treatment at the highest spatial resolution (800 particles used). The  $L_2$  norm errors based

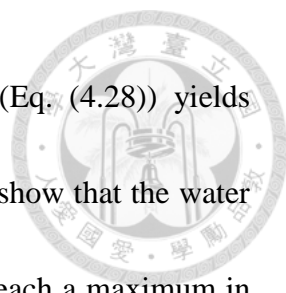




on the velocity are calculated in 41 uniform grids with a distance of 0.1 m at  $t = 60$  s (during the steady stage). Table 5.1 shows the  $L_2$  norm errors based on the velocities at different particle numbers. The  $L_2$  norm error decreases as the particle number increases. The convergence rate is 0.76, and the proposed treatment in this case is approximately convergent to  $O(\Delta x_0^{0.76})$ . The simulated SPH-SWE results for an initial particle number of 200 are presented in the following numerical accuracy discussion.

### 5.1.2 Numerical accuracies of discharge, water depth, velocity and Froude number

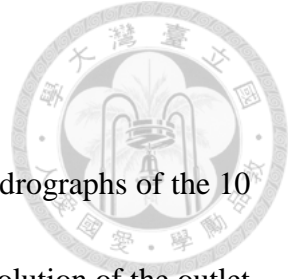
A comparison of the simulated results and data measured by Delestre *et al.* (2009) is displayed in Fig. 5.1 based on the outlet hydrograph. The simulated results exhibit good agreement with the measured data. The outlet unit discharge remains at  $6.6 \times 10^{-5}$   $\text{m}^2/\text{s}$  during the period from  $t = 60$  s to  $t = 125$  s (the so-called steady stage of the hydrograph). Thus, we present the simulated profiles of water depth, velocity and the Froude number in the flat channel at  $t = 10$  s (before the steady stage), 60 s (during the steady stage) and 160 s (after the steady stage) in Fig. 5.2 The exact solutions in the steady stage in Fig. 5.1 derived by Delestre *et al.* (2009) are also given in the figures, and the result of using the original smoothing length updating formula (Eq. (4.16)) is shown in Fig. 5.2a. Using Eq. (4.16), the error is larger when the water depth is small and the error gradually increases in the upper half of the channel. When the mass increase becomes sufficiently large, it is difficult for Eq. (4.16) to obtain the correct



solution. However, the new smoothing length updating formula (Eq. (4.28)) yields results that match the exact solutions very well. Figs. 5.2a and 5.2b show that the water depth and velocity in the channel increase before the steady stage, reach a maximum in the steady stage, and decrease after the steady stage. The simulated profiles of the Froude number shown in Fig. 5.2c indicate that the flow during the runoff process is supercritical, and the Froude number is approximately 1.5. In summary, the mass-varied particle treatment can be effectively used in the entire rainfall-runoff modeling process.

## 5.2 Nonuniform rainfall over a 1D three-slope channel

The experimental model of nonuniform rainfall over a three-slope channel proposed by Iwagaki (1955) is adopted as the second case study to explore the influences of terrain, rainfall duration and rainfall spatial distribution on the hydrograph. The configuration is given in Fig. 5.3. A 24 m-long flume with a Manning's roughness coefficient of  $0.009 \text{ sm}^{-1/3}$  is divided into three sections with equal lengths of 8 m. From the upper to lower ends, the slopes of the three sections are 0.020, 0.015 and 0.010 in sequence. Constant rainfall intensities of 389, 230 and 288 cm/hr are imposed in the upper, middle and lower sections, respectively. A fixed wall is located at the upstream boundary, and a free outflow boundary condition is specified downstream. The initial particle spacing is 0.1 m (240 particles), and an extremely small water depth of  $10^{-4}$  cm is assigned as the initial water depth of each fluid particle. Rainfall durations of 10 s, 20

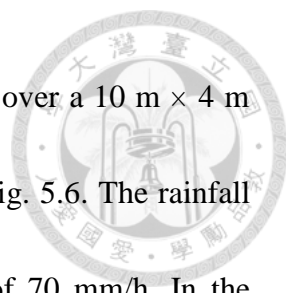


s and 30 s are considered herein.

Figures 5.4a to 5.4c give the temporal evolution of the outlet hydrographs of the 10 s, 20 s and 30 s rainfalls, and Figs. 5.4d to 5.4f show the temporal evolution of the outlet water depths associated with the 10 s, 20 s and 30 s rainfalls. The simulated results are in agreement with the measured data in both the ascending and recession limbs of the profiles. In addition, every profile of unit discharge and water depth at the outlet displays a protrusion at approximately  $t = 30$  s. The magnitude of the protrusion increases as the rainfall duration increases. The simulated results are relatively consistent with the measured data. This protrusion is formed when the upstream flow with a larger momentum catches up to the downstream flow with a smaller momentum. At the location of the flow convergence, the water depth increases abruptly, which results in the formation of protrusions in the outlet hydrograph and the water depth profile. Figures 5.5a to 5.5c then illustrate the temporal evolution of the Froude number at the outlet for 10 s, 20 s and 30 s rainfalls. The outlet flows of the three rainfall durations change from subcritical to supercritical at approximately  $t = 10$  s. Overall, the new proposed treatment exhibits good performance for the problem of nonuniform rainfalls of different rainfall durations over a 1D three-slope channel.

### **5.3 Uniform rainfall over a 2D plot with complex topography**

In the third case, the proposed treatment is validated based on a rainfall experiment

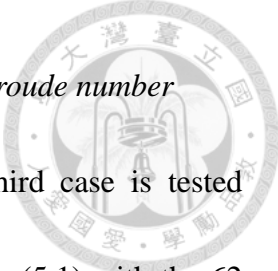


performed by Tatard *et al.* (2008). This experiment was carried out over a 10 m × 4 m plot with a slope of 1% in the longitudinal direction, as shown in Fig. 5.6. The rainfall duration was 2 hours and 15 minutes, with a constant intensity of 70 mm/h. In the numerical simulations, a Manning's roughness coefficient of 0.02  $\text{sm}^{-1/3}$  is used to calculate the bed friction imposed on the fluid particles. A fixed wall is established at the upstream boundary, and a free outflow boundary condition is established downstream. An extremely small water depth of  $10^{-4}$  m is prescribed as the initial water depth of each fluid particle.

### 5.3.1 Convergence analysis of the particle number

Five initial particle numbers of 1,000, 4,000, 16,000, 64,000 and 256,000 (i.e., initial particle spacings  $\Delta x_0$  of 0.2, 0.1, 0.05, 0.025 and 0.0125 m, respectively) are adopted to perform the convergence analysis. The reference velocities are obtained by the proposed treatment at a highest spatial resolution (256,000 particles used) to calculate the  $L_2$  norm errors based on the water velocity using Eq. (5.1). The  $L_2$  norm errors of different particle numbers are calculated in 189 uniform grids with a distance of 0.5 m, and the errors are presented in Table 5.2. The  $L_2$  norm error decreases as the particle number increases. The convergence rate based on the velocity is 1.38. The proposed treatment for this case is approximately convergent to  $O(\Delta x_0^{1.38})$ . The simulated results based on 16,000 particles are then used to analyze the accuracy.

### 5.3.2 Numerical accuracies of discharge, water depth, velocity and Froude number



The numerical accuracy of the proposed treatment for the third case is tested against the measured velocities of Tatard *et al.* (2008). Applying Eq. (5.1) with the 62 measured velocities, the  $L_2$  norm error based on the velocity is 0.0982. Figure 5.7 shows the correlation between the simulated and measured velocities. The velocities simulated using the proposed treatment exhibit good agreement with the measured velocities.

We also compare the proposed SPH-SWEs treatment to two mesh-based schemes. One is a finite difference method (FDM) adopted by Tatard *et al.* (2008), and the other is a Mixed-Hybrid Finite Element method (MHFEM) applied by Mügler *et al.* (2011). The  $L_2$  norm errors based on the velocities determined using the FDM and the MHFEM are both 0.1200. Therefore, the present study provides better numerical accuracy compared to the two mesh-based schemes.

In addition, Figures 5.8a to 5.8c present the simulated contours of water depth, velocity and Froude number. The deeper the water depth is, the larger the velocity in the main rill, as shown in Figs. 5.8a and 8b. Fig. 5.8c shows that the runoff includes mixed flow regimes of both subcritical and supercritical flows. Most of the subcritical flows are distributed in the upper half of the runoff area, while the flows in the main rill are supercritical. The higher Froude numbers appear in the offshoots of the rill. Here, we show the capacity of SPH modeling with mixed flow regimes caused by rainfall over

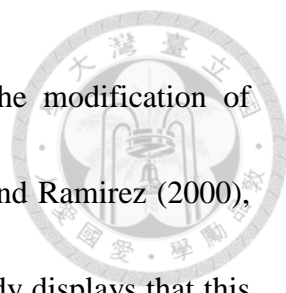
complex terrain.

## 5.4 Green-Ampt infiltration



Previous three case studies are the situations of fluid mass addition, and this forth is conducted to test the situation of fluid mass reduction. This overland flow with infiltration event on a plane was first carried out by Woolhiser *et al.* (1996). Green-Ampt infiltration model is adopted for the simulations and the related parameters are given as follows: the wetting front suction  $\Psi = 44$  cm, the volumetric moisture content deficit (capacity minus initial) at the wetting front  $\Delta\theta = 0.25$  and the effective hydraulic conductivity  $K_s = 3.53 \times 10^{-4}$  cm/s (Fiedler and Ramirez, 2000). The rainfall intensity is 177.6 mm/h, and the rainfall duration is 20 min. The plane is 50 m-long and 20 m-wide with bed slope = 0.04 and its Manning friction coefficient is  $0.1 \text{ sm}^{-1/3}$ . The numerical simulation was performed using initial particle spacing  $\Delta x_0 = \Delta y_0 = 0.25$  m and initial time step  $\Delta t_0 = 0.1$  s.

The simulated discharge at the outlet of plane is displayed in Fig. 5.9 and compared with the outcome of Fiedler and Ramirez (2000). In general the two results are close except the peak values. In 2D SPH-SWEs model the discharge is obtained by averaged integral over the variables of  $(u, v, d_w)$  while the values of  $(u, v, d_w)$  at certain location is calculated with SPH kernel interpolation. Not only the simulated values of  $(u, v, d_w)$  are affected by the wall boundary condition but also the support domain of the



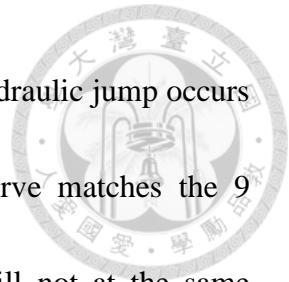
kernel interpolation is truncated by the wall boundary even if the modification of truncation is given. Thus comparing with the 1D result of Fiedler and Ramirez (2000), the 2D result with SPH-SWEs has lower peak values. This case study displays that this mass-varied SPH-SWEs model can correctly handle the fluid mass addition and reduction at the same time.

### 5.5 1D pipe flow with SPH-SWEs

In this section the basic ability of the 1D SPH-SWEs for sewer module is examined. This is a 1D steady case that both the free surface flow and pressurized flow are coexisted and contacted by a hydraulic jump. A pipe with constant cross-sectional circular area has three parts from the upstream end to the downstream end: a 2 m-long horizontal section, a 4 m-long inclined section with an angle  $10^\circ$  between the horizontal line and a 2 m-long horizontal section. The inner diameter of the pipe is 0.22 m. A constant inflow discharge  $0.03 \text{ m}^3/\text{s}$  is preserved at the inlet of the upstream end and a constant piezometric head 0.554 m is imposed as the downstream end boundary condition. The Manning friction coefficient is zero  $\text{sm}^{-1/3}$  (Aldrighetti, 2007; Casulli and Stelling, 2013). The initial particle spacing  $\Delta x_0$  is 0.01 m and the initial time step  $\Delta t_0$  is 0.003 s.

Figure 5.10 demonstrates the simulated result of SPH-SWEs. The upstream end of the pipe is a free surface flow with the water depth around 0.15 m. The water flows

along the pipe and chokes at the downstream end around which a hydraulic jump occurs and the flow becomes a pressurized flow. The water surface curve matches the 9 experimental measured points. However the hydraulic jump is still not at the same position of the experiment result (Aldrighetti, 2007). Basically this 1D SPH-SWEs sewer module is fine but still needs modifications for the better performance and more tests for verification. For the ongoing work, the mass transfer mechanism between the 2D rainfall-runoff module and the 1D sewer module will be developed.





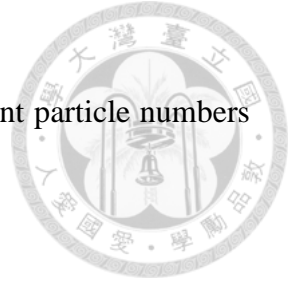


Table 5.1

The  $L_2$  norm errors based on the velocity at  $t = 60$  s for four different particle numbers in the first case study.

Number of particles	$L_2$ norm error
(1) 50	0.0711
(2) 100	0.0613
(3) 200	0.0506
(4) 400	0.0131
(5) 800	-

Table 5.2

The  $L_2$  norm errors based on the velocity for four different particle numbers in the third case study.

Number of particles	$L_2$ norm error
(1) 1000	1.0002
(2) 4000	0.9175
(3) 16000	0.5658
(4) 64000	0.0490
(5) 256000	-

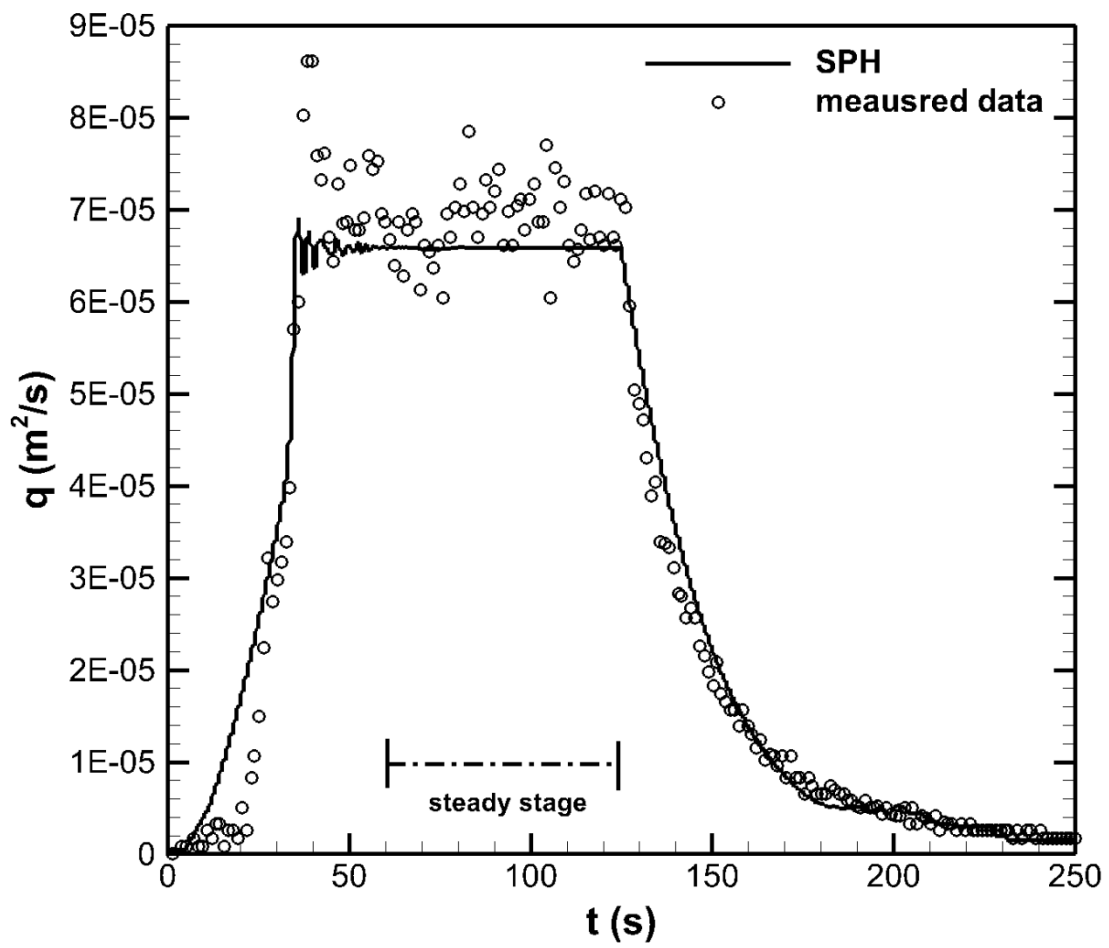


Fig. 5.1 The simulated and measured hydrographs of the case study in section 5.1.

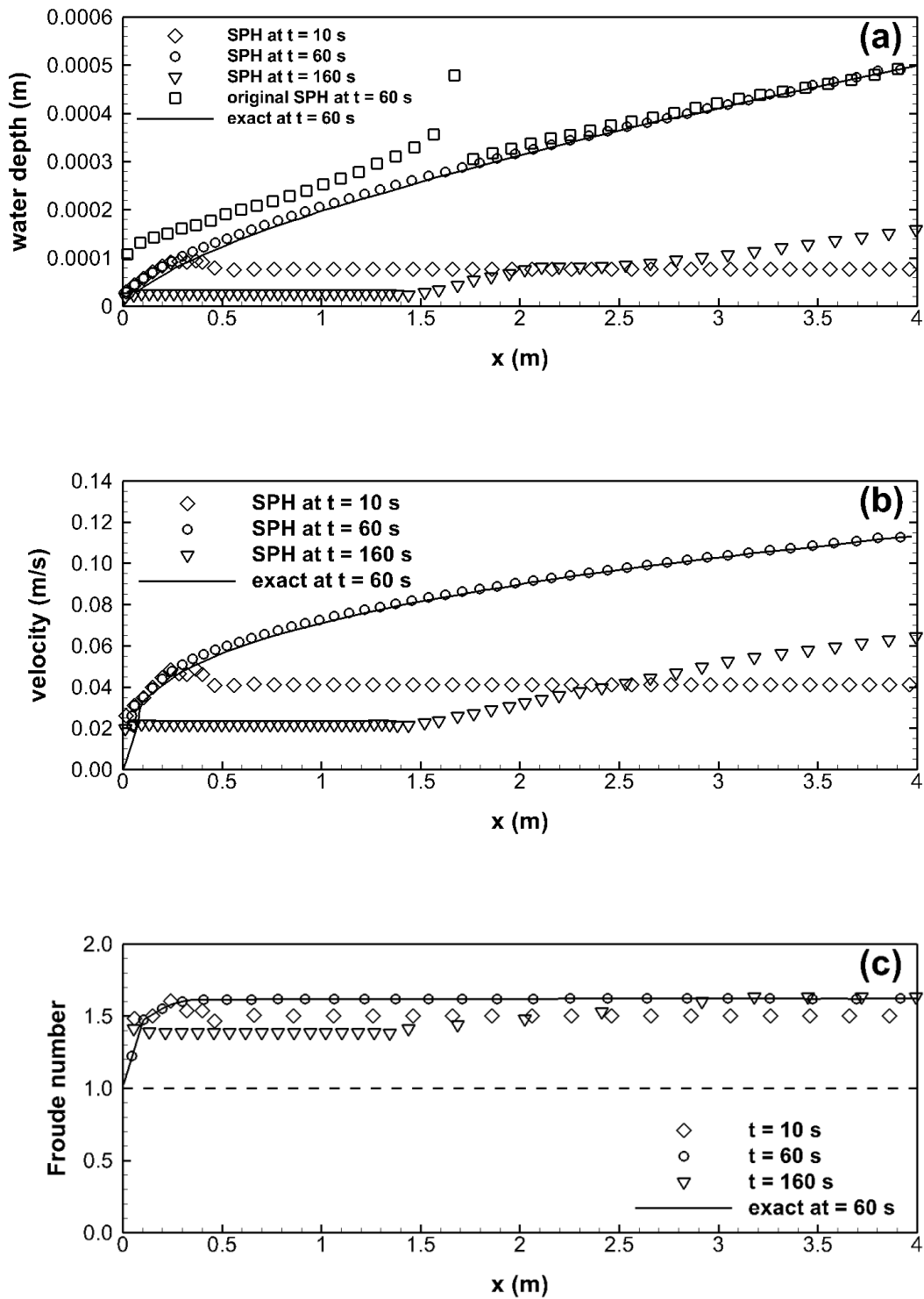
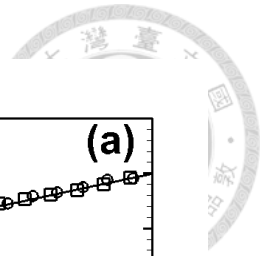


Fig. 5.2 The simulated profiles of (a) water depth, (b) velocity and (c) Froude number along the channel at  $t = 10$  s, 60 s and 160 s in the case study in section 5.1.

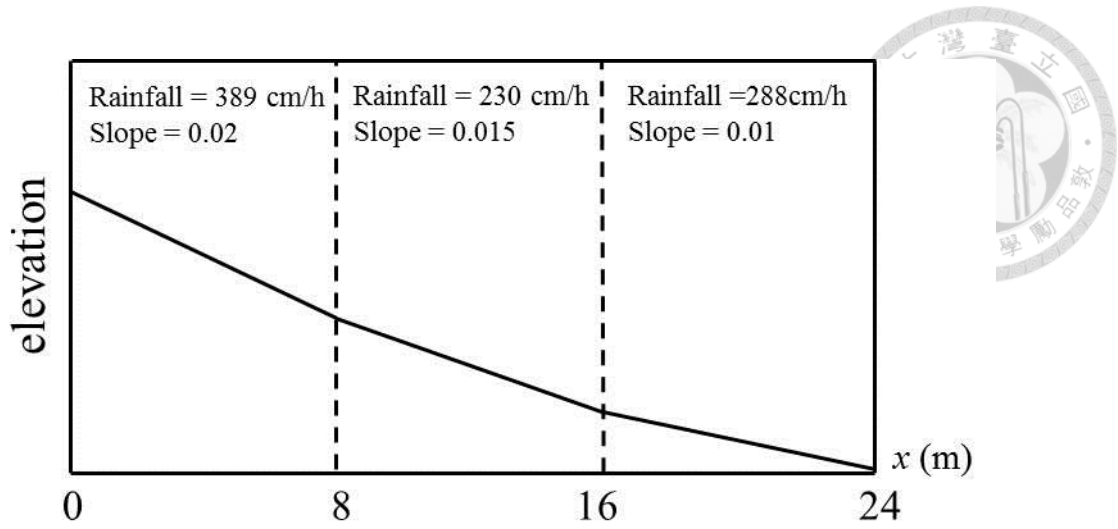


Fig. 5.3 The profile of bed elevation of the case study in section 5.2.

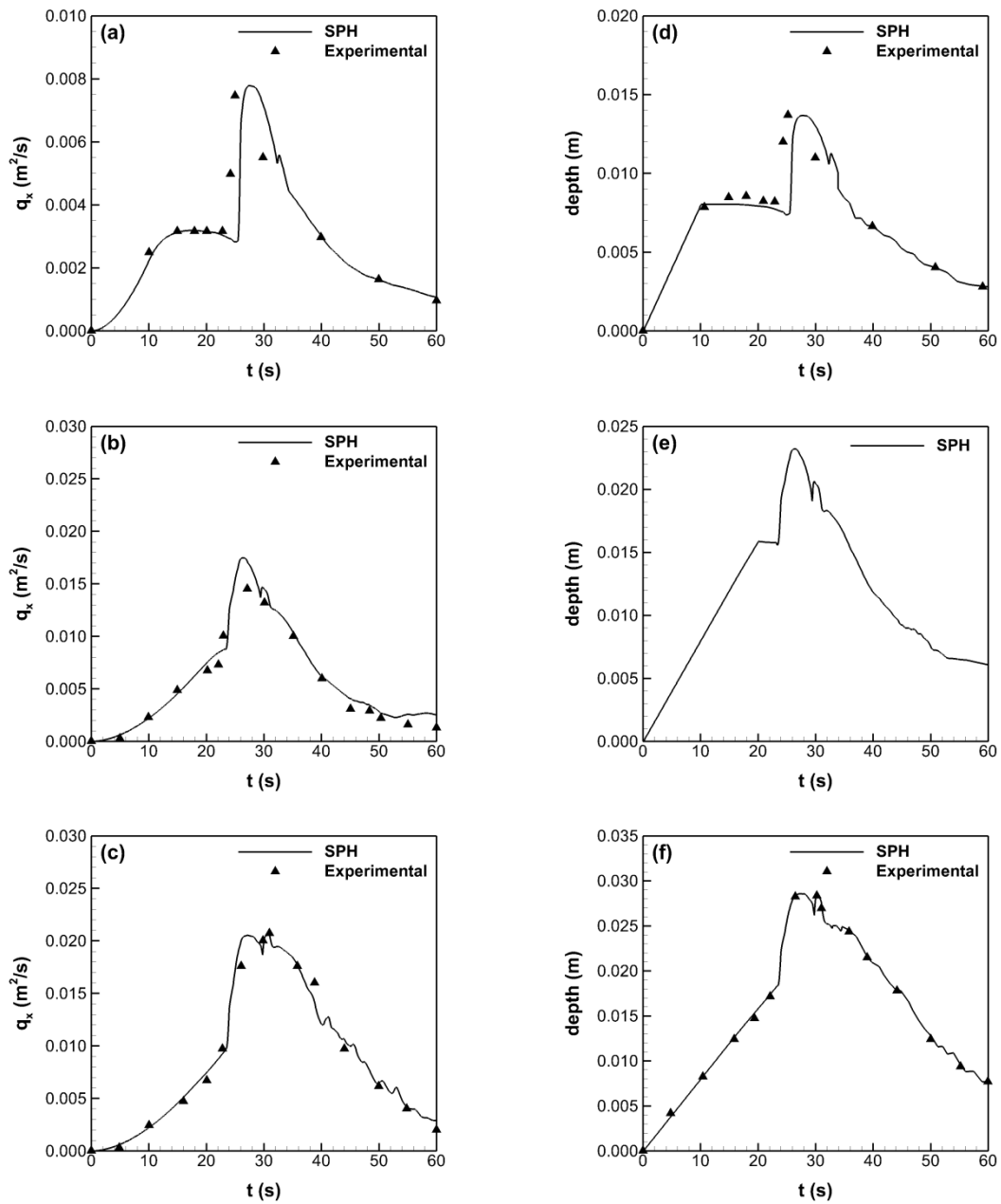


Fig. 5.4 The simulated hydrography and the simulated profiles of water depth in the case study in section 5.2, (a) and (d) rainfall duration = 10 s, (b) and (e) rainfall duration = 20 s and (c) and (f) rainfall duration = 30 s.

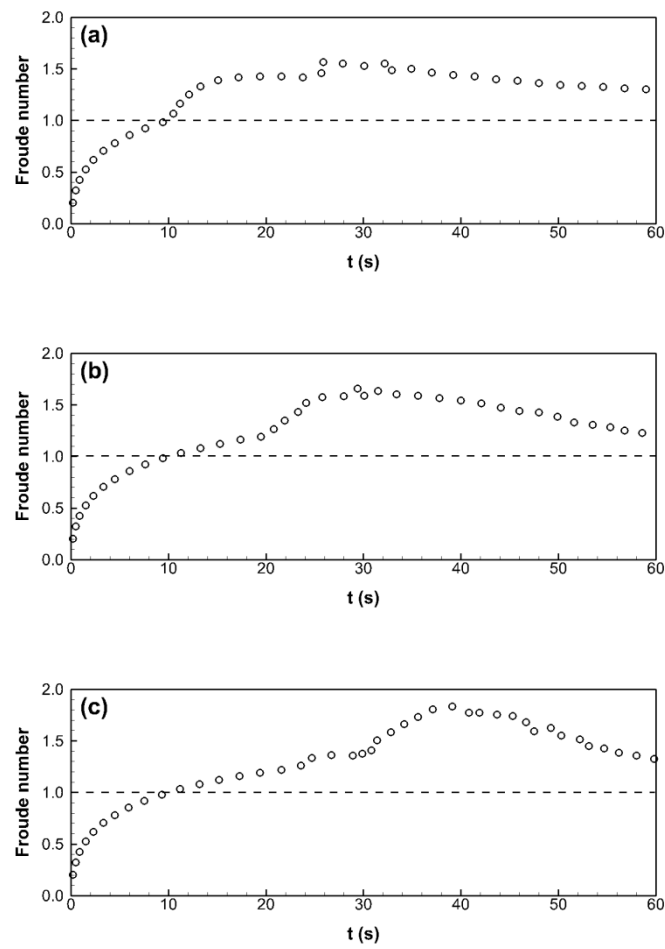


Fig. 5.5 The temporal evolution of the Froude number at the outlet of the second case study, (a) a rainfall duration = 10 s, (b) rainfall duration = 20 s and (c) rainfall duration = 30 s.

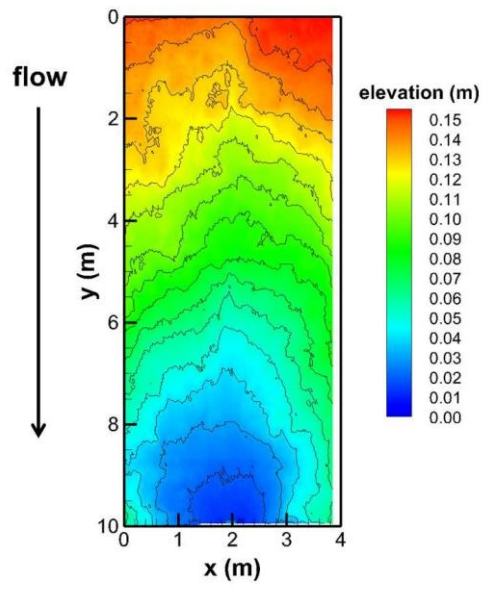


Fig. 5.6 The topography of the 2D plot of the case study in section 5.3.

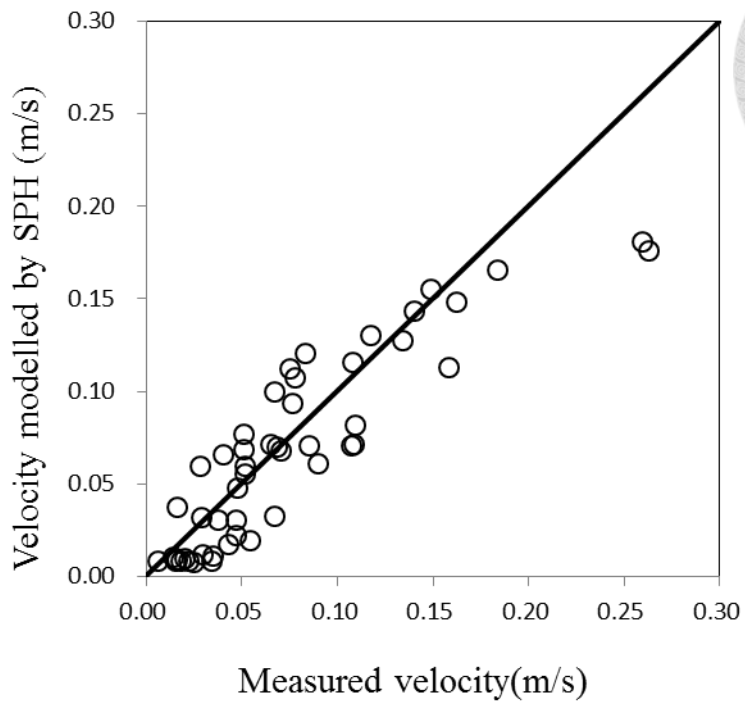


Fig. 5.7 The correlation between the simulated and measured velocities at the 62 measured points of the case study in section 5.3.



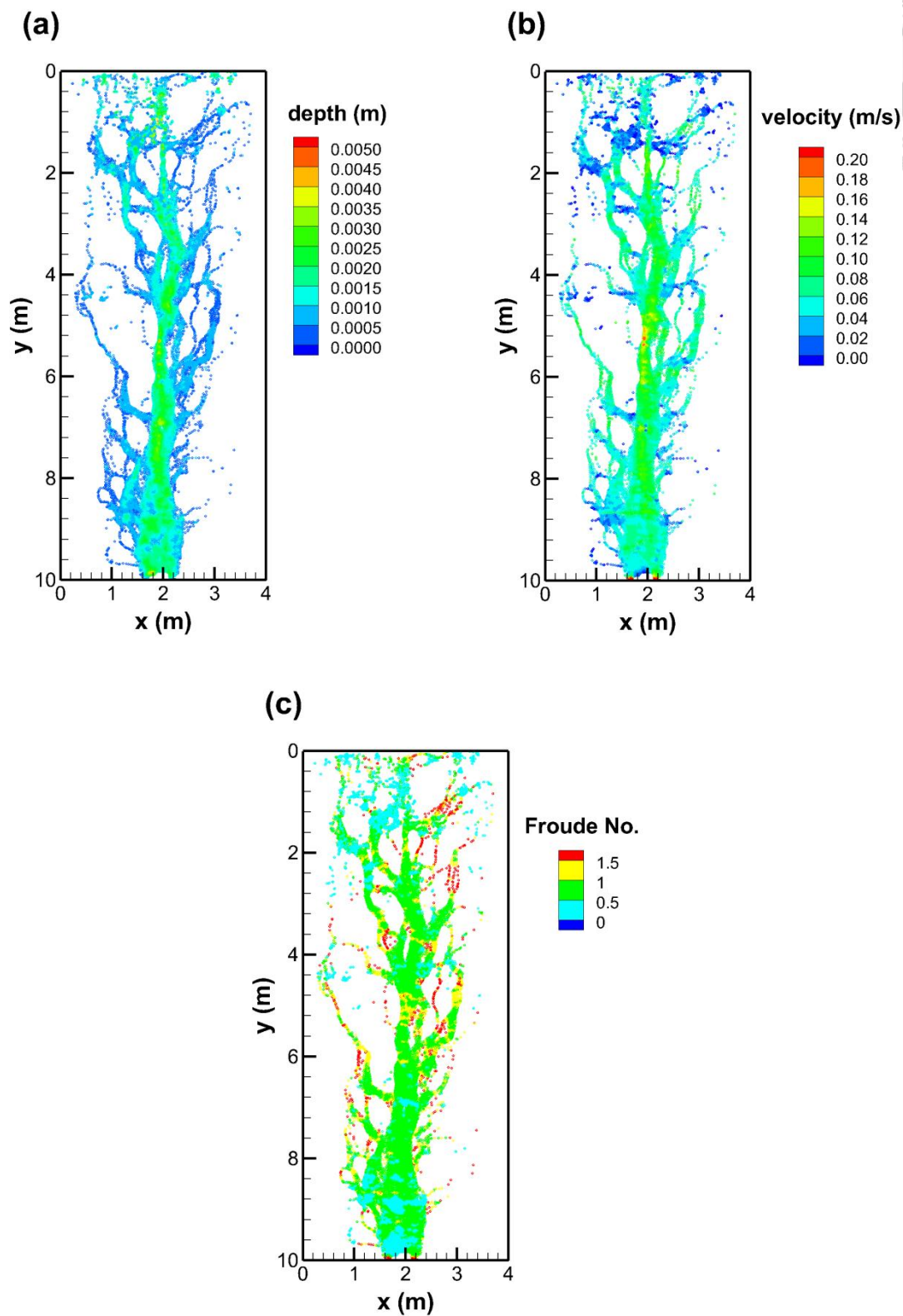


Fig. 5.8 The simulated contours of water depth, velocity and Froude number of the case study in section 5.3.

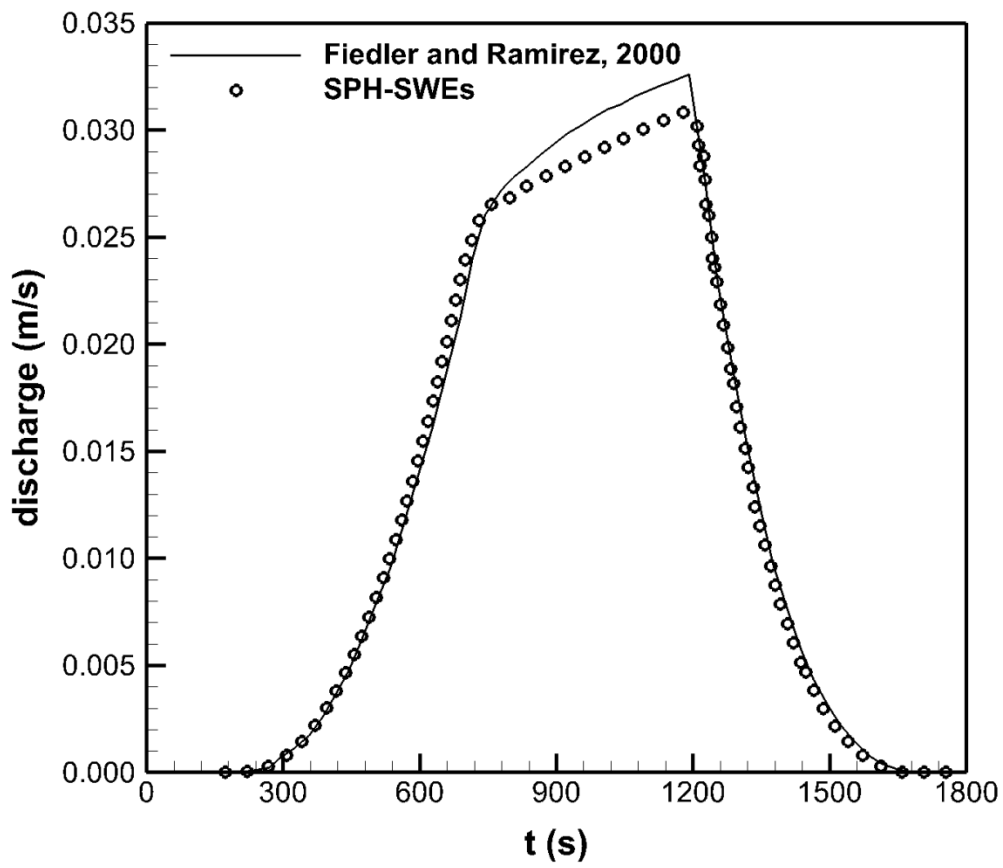


Fig. 5.9 The simulated discharge by SPH-SWEs with Green-Apmt infiltration.

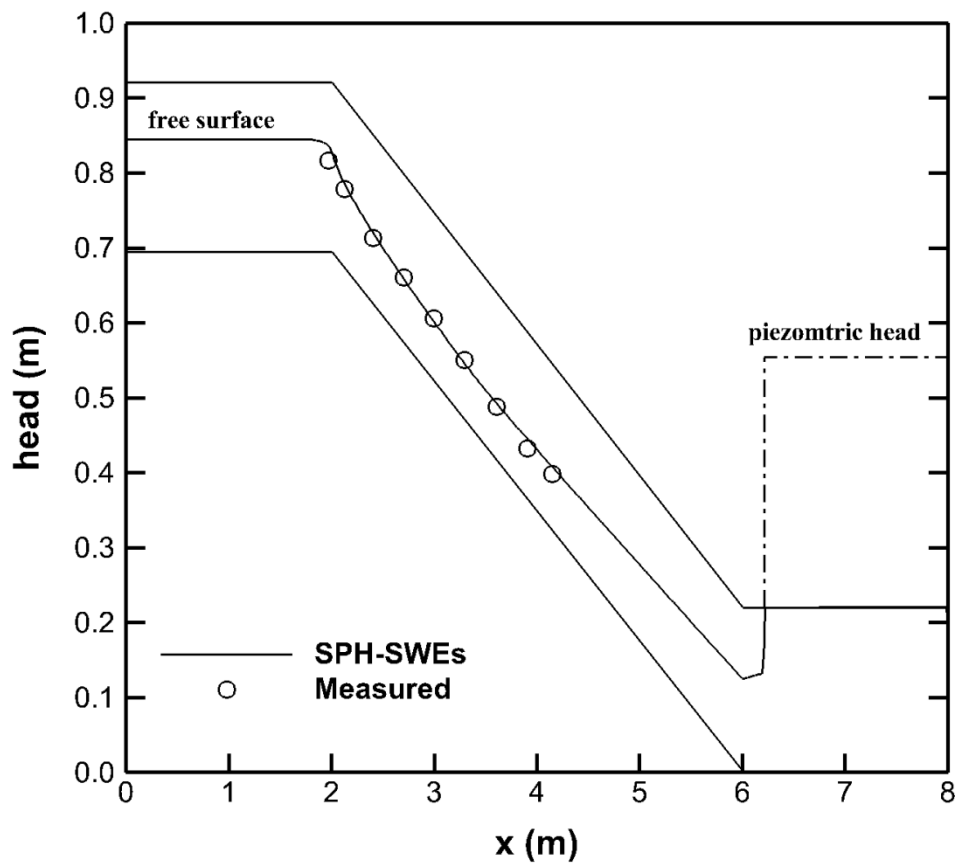
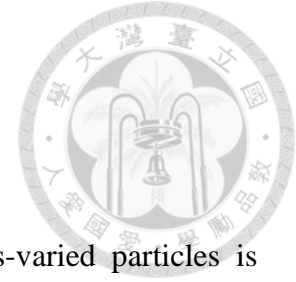


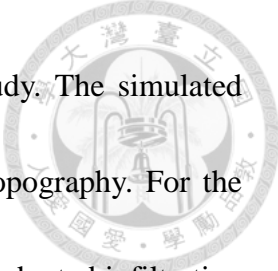
Fig. 5.10 The simulated result of SPH-SWEs for 1D pipe flow with TPA.



## Chapter 6 Conclusions

In this thesis, a novel SPH-SWEs treatment that uses mass-varied particles is developed to model the rainfall-runoff process. Mass-varied particles are used for the first time in SPH to simulate mass-varied systems. To obey the conservation laws during a rainfall event, the particle mass should vary. Furthermore, by changing the mass of the released particles, additional particles do not need to be added, as the total mass of the system increases during the simulations. Evaluating water depths via iterations can also avoid solving additional source terms of mass variation. However, the original smoothing length update formula yields incorrect values, as the change in water depth is caused by mass variations instead of changes in the relative particle positions. Therefore, a modified smoothing length updating formula is derived based on different assumptions. The combined use of mass-varied particles and the modified smoothing length formula for modeling rainfall-runoff processes is the major focus of this thesis.

Three benchmark case studies and two applications are then used to assess the abilities of the proposed treatment. The numerical results demonstrate that the outlet hydrograph, water depth and velocity field exhibit good agreement with the exact solutions and experimental data. Additionally, the proposed treatment can address every stage of uniform/nonuniform rainfall events. The runoff “catch-up” phenomenon due to



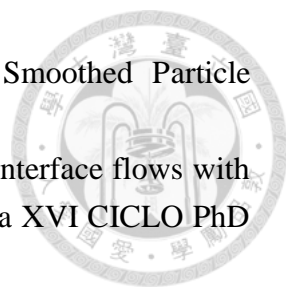
the difference in flow momentums can also be observed in the study. The simulated Froude numbers are reasonably predicted, even for complex bed topography. For the modeling of fluid reduction during the rainfall-runoff processes, the adopted infiltration model has good performance with mass-varied SPH-SWEs. The basic functions of the 1D sewer module have also been constructed although modifications are still needed for improvements. The mass transfer mechanism between the 2D rainfall-runoff module and the 1D sewer module is an ongoing work for the future study. In general it can be concluded that the robustness and reliability of the newly proposed SPH-SWEs treatment have been proven for modeling rainfall-runoff processes in the presence of hydraulic jumps, dry/wet bed flows and supercritical/subcritical/transcritical flows. As a result, this study has extended the range of SPH-SWEs applications from only modeling discharge flows in open channels or floodplains without rainfall to modeling rainfall-runoff processes in watersheds.



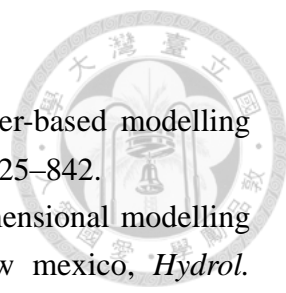
## References


- Aldrighetti E., Computational hydraulic techniques for the Saint Venant Equations in arbitrary shaped geometry, *Ph.D thesis*, Department of Mathematics, University of Trento, 2007.
- Amicarelli A., Marongiu J.C., Leboeuf F., Leduc J. and Caro J., SPH truncation error in estimating a 3D function, *Comput. Fluids* 2011; **44**:279-296.
- Ata R. and Soulaïmani A., A stabilized SPH method for inviscid shallow water flows, *Int. J. Numer. Meth. Fluids* 2005; **47**:139-159.
- Bates P.D., Marks K.J. and Horrit M.S., Optimal use of high-resolution topographic data in flood inundation models. *Hydrol. Process.* 2003; **17**:5237–5257.
- Benz W., Smooth particle hydrodynamics - a review. In Robert J. Buchler, editor, *Proceedings of the NATO Advanced Research Workshop on The Numerical Modelling of Nonlinear Stellar Pulsations Problems and Prospects*. Kluwer Academic Publishers, 1990.
- Beven K.J., *Rainfall-Runoff Modelling: The Primer*. John Wiley & Sons Ltd., Chichester, 2001.
- Bonet J. and Kulasegaram S., Correction and stabilization of smoothed particle hydrodynamics methods with applications in metal forming simulations, *Int. J. Numer. Meth. Eng.* 2000; **47(6)**: 1189-1214.
- Bonet J., Kulasegaram S., Rodriguez-Paz M.X. and Profit M., Variational formulation for the smooth particle hydrodynamics (SPH) simulation of fluid and solid problems. *Comput. Meth. Appl. Mech. Engrg.* 2004; **193**:1245-56.
- Bonet J. and Lok T-S L., Variational and momentum preservation aspects of smooth particle hydrodynamic formulations, *Comput. Methods Appl. Mech. Eng.* 1999; **180**:97-115.
- Borve S., Omang M. and Trulsen J., Regularized smoothed particle hydrodynamics: A new approach to simulating magnetohydrodynamics shocks, *Astrophys J.* 2001; **561(1)**: 82-93.
- Bourdarias C. and Berbi S., A finite volume scheme for model coupling free surface and pressurised flows in pipes, *J. Comput. Appl. Math.* 2007; **209**:109-131.
- Bouso S., Daynou M. and Fuamba M., Numerical modeling of mixed flows in storm water systems: critical review of literature, *J. Hydraul. Eng.* 2013; **139(4)**:385-396.
- Caia Li, Fengb J.H., Xiec W.X. and Zhoua J., Computations of steady and unsteady transport of pollutant in shallow water, *Math Comput. Simulat.* 2006; **71**:31-43.
- Casulli V. and Stelling G.S., A semi-implicit numerical model for urban drainage

- systems, *Int. J. Numer. Methods Fluids* 2013; **73**:600-614.
- Cea L., French J. and Vázquez-Cendón M.E., Numerical modelling of tidal flows in complex estuaries including turbulence: an unstructured finite volume solver and experimental validation, *Int. J. Numer. Methods. Eng.* 2006; **67(13)**:1909–1932.
- Cea L., Puertas J., and Vázquez-Cendón M.E., Depth averaged modelling of turbulent shallow water flow with wet–dry fronts., *Arch. Comput. Methods Eng. (ARCME)* 2007;**14 (3)**.
- Cea L., Garrido M. and Puertas J., Experimental validation of two-dimensional depth-averaged models for forecasting rainfall–runoff from precipitation data in urban areas, *J. Hydrol.* 2010; **382**:88-102.
- Chahinian N., Moussa R., Andrieux P. and Voltz M., Comparison of infiltration models to simulate flood events at the field scale, *J. Hydrol.* 2005; **306**:191-214.
- Chaniotis A.K., Poulidakos D. and Koumoutsakos P., Remeshed smoothed particle hydrodynamics for the simulation of viscous and heat conducting flows. *J. Comput. Phys.* 2002; **180**:67-90
- Chang K.H., Kao H.M., and Chang T.J., Lagrangian modeling of particle concentration distribution in indoor environment with different kernel functions and particle search algorithms, *Buildi. Environ.* 2012; **57**:81-87.
- Chang T.J., Kao H.M. , Chang K.H., and Hsu M.H., Numerical Simulation of Shallow-Water Dam Break Flows in Open Channels Using Smoothed Particle Hydrodynamics, *J. Hydrol.* 2011; **408**:78-90.
- Chang T.J. and Chang K.H., SPH modeling of one-dimensional nonrectangular and nonprismatic channel flows with open boundaries, *J. Hydraul. Eng.* 2013; **139(11)**:1142-1149.
- Chang T.J., Chang K.H., Kao H.M., and Chang Y.S., Comparison of a New Kernel Method and a Sampling Volume Method for Estimating Indoor Particulate Matter Concentration with Lagrangian Modeling, *Build. Environ.* 2012; **54**: 20-28.
- Chang T.J., Chang Y.S. and Chang K.H., Modeling rainfall-runoff processes using smoothed particle hydrodynamics with mass-varied particles, *J. Hydrol.* 2016; **543**: 749-758.
- Chang Y.S. and Chang T.J., SPH simulation of solute transport in flows with steep velocity and concentration gradients, *Water* 2017; **9**: 132-149.
- Chen L. and Young M.H., Green-Ampt infiltration model for sloping surface, *Water Resour. Res.* 2006; **42**, doi:10.1029/2005WR004468.
- Chow V.T., Maidment D., and Mays L., Applied Hydrology. McGraw-Hill, New York, 1988.
- Cleary P.W., Modeling Confined Multi-material Heat and Mass Flows Using SPH, *Appl. Math Model.* 1998; **22**:981-993.

- 
- Cleary P.W. and Monaghan J.J., Conduction Modelling Using Smoothed Particle Hydrodynamics, *J. Comp. Phys.* 1999; **148**:227-264.
- Colagrossi A., A meshless Lagrangian method for free-surface and interface flows with fragmentation, Dottorato di Ricerca in Meccanica ed Applicata XVI CICLO PhD Thesis, Universtia di Roma, La Sapienza, 2004.
- Colagrossi A. and Landrini M., Numerical simulation of interfacial flows by smoothed particle hydrodynamics, *J. Comp. Phys.* 2003; **191**:448-475.
- Costabile P., Costanzo C. and Macchione, F., A storm event watershed model for surface runoff based on 2D fully dynamic wave equations, *Hydrol. Process* 2013; **27**:554-569.
- Delestre O., Cordier S., James F. and Darboux F., Simulation of rainwater overland-flow. In Proceedings of the 12th International Conference on Hyperbolic Problems, Proceedings of Symposia in Applied Mathematics, Amer. Msth: University of Maryland, College Park (USA). 2009; **67**:537–546.
- Delestre O., Darboux F., James F., Lucas C., Laguerre C. and Cordier S., FullSWOF: A free software package for the simulation of shallow water flows, arXiv:1401.4125.
- de Lefte M., le Touzé D. and Alessandrini B., SPH modeling of shallow-water coastal flows, *J. Hydraul. Res. Extra Issue* 2010; **48**:118-125.
- Dilts G.A., Moving least squares hydrodynamics: consistency and stability, *Int. J. Numer. Methods* 1999; **44**:1115-1155.
- Esteves M., Faucher X., Galle S., and Vauclin M., Overland flow and infiltration modeling for small plots unsteady rain: numerical results versus observed values, *J. Hydrol.* 2000; **228**:265-282.
- Fiedler F.R. and Ramirez J.A., A numerical method for simulating discontinuous shallow flow over an infiltrating surface, *Int. J. Numer. Methods Fluids* 2000; **32**:219-240.
- Federico I., Marrone S., Colagrossi A., Aristodemo F. and Antuono M., Simulating 2D open-channel flows through an SPH model, *Eur. J. Mech. B-Fluid* 2012; **34**:35-46.
- Ferrari A., Dumbser M., Toro E.F. and Armanini A., A new 3d parallel SPH scheme for free surface flows, *Comput. Fluids* 2009; **38(6)**:1203–1217.
- Freeze R.A., and Harlen R.L., Blueprint for a physically-based digitally simulated hydrological response model, *J. Hydrol.* 1969; **9**:237–258.
- Fulk D.A. and Quinn D.W., An analysis of 1-D smoothed particle hydrodynamics kernels, *J. Comput. Phys.* 1996; **126(1)**:165-180.
- Gingold R.A. and Monaghan J.J., Smoothed Particle Hydrodynamics: Theory and Application to Non-spherical stars, *Monthly Notices of the Royal Astronomical Society* 1977; **181**:375-389.
- Gingold R.A. and Monaghan J.J., Kernel estimate as a basis for general particle method



- 
- in hydrodynamics, *J. Comp. Phys.* 1982; **46**:429-453.
- Horrit M.S. and Bates P.D., Predicting floodplain inundation: raster-based modelling versus the finite-element approach, *Hydrol. Process.* 2001; **15**:825–842.
- Howes D.A., Abrahams A.D. and Pitman, E.B., One- and two-dimensional modelling of overland flow in semiarid shrubland, jornada basin, new mexico, *Hydrol. Process.* 2006; **20**:1027–1046.
- Hung W.C., A new SPH-SWE approach for modeling of lateral flows in open-channels, Mater Thesis, 2014.
- Hunter N.M., Bates P.D., Horritt M.S. and Wilson M.D., Simple spatiallydistributed models for predicting flood inundation: a review, *Geomorphology* 2007; 90: 208–225.
- Iwagaki Y., Fundamental studies on runoff analysis by characteristics. Disaster Prev. Res. Inst., Kyoto Univ., Kyoto, Japan, 1955, Bull **10**:1-25.
- Jian W., Liang D., Shao S., Chen R. and Liu, X., SPH study of the evolution of water–water interfaces in dam break flows, *Nat. Hazards.* 2015; **78**(1):531-553.
- Kao H.M. and Chang T.J., Numerical modeling of dambreak-induced flood and inundation using smoothed particle hydrodynamics, *J. Hydrol.* 2012; **448-449**:232-244.
- Kivva S.L. and Zheleznyak M.J., Two-dimensional modeling of rainfall runoff and sediment transport in small catchments areas, *Int. J. Fluid Mech. Res.* 2005; **32** (6):703 – 716.
- Liang D.F., Lin B.L. and Falconer R.A., Simulation of rapidly varying flow using an efficient TVD-MacCormack scheme, *Int. J. Numer. Meth. Fluids* 2007; **53**:811-826.
- Libersky L.D., Petschek A.G., Carney T.C., Hipp J.R. and Allahdadi F.A., High-strain Lagrangian hydrodynamics – a 3-dimensional SPH code for dynamic material response, *J. Comput. Phys.* 1993; **109**(1):67-75.
- Liu G.R. and Liu M.B., Smoothed Particle Hydrodynamics, *World Scientific Publishing Co. Pte. Ltd*, 2003.
- Liu Q.Q., Chen L., Li J.C. and Singh V.P., Two-dimensional kinetic wave model of overland-flow, *J. Hydrol.* 2004; **291**:28-41.
- Lo E.Y.M. and Shao S., Simulation of near-shore solitary wave mechanics by an incompressible SPH method, *Applied Ocean Research* 2002; **24**:275-286.
- Lucy L.B., Numerical approach to testing the fission hypothesis, *Astronomical Journal* 1977; **82**:1013-1024.
- Macdonald I., Baines M.J., Nichols N.K., and Samuels P.G., Analytic benchmark solutions for open channel flows, *J. Hydraul. Eng.* 1997; **123**: 1041-1045.
- Mein R.G. and Larson C.L., Modeling infiltration during a steady rain, *Water Resour.*

- 
- Res. 1973; **9(2)**:384-394.
- Mignot E., Paquier A. and Haider S., Modeling floods in a dense urban area using 2D shallow water equations, *J. Hydrol.* 2006; **327 (1–2)**:186–199.
- Monaghan J.J., Why particle methods work (hydrodynamics), *SIAM Journal on Scientific and Statistical Computing* 1982; **3**:422-433.
- Monaghan J.J., Particle methods for hydrodynamics, *Computer Physics Report* 1985; **3**:71-124.
- Monaghan J.J., An introduction to SPH, *Comput. Phys. Commun.* 1988; **48**:89-96.
- Monaghan J.J., On the problem of penetration in particle methods, *J. Comp. Phys.* 1989; **82**:1-15.
- Monaghan J.J., Simulating free surface flows with SPH, *J. Comp. Phys.* 1994; **110**:399-406.
- Monaghan J.J., Heat condition with discontinuous conductivity, *Applied Mathematics Reports and Preprints*, Monash University, (95/18), 1995b.
- Monaghan J.J., SPH and Riemann solver, *J. Comp. Phys.* 1997; **136**:298-307.
- Monaghan J.J., SPH compressible turbulence, *Mon. Not. R. Astron. Soc.* 2002; **335**:843-852.
- Monaghan J.J., Smoothed Particle Hydrodynamics, *Rep. Prog. Phys.* 2005; **68**:1703-1759.
- Monaghan J.J. and Gingold R.A., Shock simulation by the particle method of SPH, *J. Comp. Phys.* 1983; **52**:374-381.
- Monaghan J.J. and Kajtar J., SPH particle boundary forces for arbitrary boundaries., *Comput. Phys. Commun.* 2009; **180(10)**:1811–1820.
- Monaghan J.J. and Kos A., Solitary waves on a Cretan beach, *J. Waterway Port, Coastal and Ocean Engrg* 1999; **125**:145-154.
- Monaghan J.J., Kos A. and Issa N., Fluid motion generated by impact, *J. Waterway Port Coastal Ocean Eng.* 2004; **139**:250-259.
- Monaghan J.J. and Kocharyan A., SPH simulation of multi-phase flow, *Comput. Phys. Commun.* 1995; **87**:225-235.
- Monaghan J.J. and Lattanzio J.C., A refined method for astrophysical problems, *Astron. Astrophys.* 1985; **149**:135-143
- Morris J.P., Analysis of smoothed particle hydrodynamics with applications, *Ph. D thesis*, Monash University, 1996.
- Morris J.P., Zhu Y. and Fox P.J., Parallel simulation of pore-scale flow through porous media, *Comput. Geotech.* 1999; **25**:227-246.
- Mügler C., Planchon O., Patin J., Weill S., Silvera N., Richard P. and Mouche E., Comparison of roughness models to simulate overland flow and tracer transport experiments under simulated rainfall at plot scale, *J. Hydrol.* 2011; **402(1–2)**:25–

40.

- Price D.J., Smoothed particle hydrodynamics and magnetohydrodynamics, *J. Comput. Phys.* 2012; **231(3)**:759-794.
- Price D.J. and Monaghan J.J., Smoothed particle magnetohydrodynamics: I. Algorithms and tests in one dimension, *Mon. Not. R. Astron. Soc.* 2004; **348**:123-138.
- Pu J.H., Shao S., Huang Y. and Hussain K., Evaluations of SWEs and SPH numerical modelling techniques for dam break flows, *Eng. Appl. Comp. Fluid* 2013; **7(4)**: 544-563.
- Quinlan N.J., Basa M. and Lastiwka M., Truncation error in mesh-free particle methods, *Int. J. Numer. Meth. Eng.* 2006; **66(13)**: 2064-2085.
- Quirk J.J., A contribution to the great Riemann solver debate, *Int. J. Numer. Methods Fluids* 1994; **18**:555-574.
- Randles P.W. and Libersky L.D., Smoothed particle hydrodynamics: some recent improvements and applications, *Comput. Method Appl. M* 1996; **139**:375-408.
- Rhoades C.E., A fast algorithm for calculating particle interactions in smooth particle hydrodynamics simulations, *Comput. Phys. Commun.* 1992; **70**: 478-482.
- Rodriguez-Paz M.X. and Bonet J., A corrected smooth particle hydrodynamics formulation of the shallow-water equations, *Comput. Struct.* 2005; **83**:1396-1410.
- Sanders B.F. and Bradford S.F., Network implementation of the two-component pressure approach for transient flow in storm sewers, *J. Hydraul. Eng.* 2011; **137(2)**: 158-172.
- Shao S. and Lo E.Y.M., Incompressible SPH method for simulating Newtonian and non-Newtonian flows with a free surface, *Adv. Water Resour.* 2003; **26(7)**:787-800.
- Singh J., Altinakar M.S. and Ding Y., Numerical modeling of rainfall-generated overland flow using shallow-water equations, *J. Hydrol. Eng.* 2014, doi:10.1061/(ASCE)HE.1943-5584.0001124.
- Soares-Frazão S., and Testa G., The Toce river test case: numerical results analysis. In: Proceedings of the 3rd CADAM Workshop, Milan, Italy, 1999.
- SPHERIC: David Le Touzé, retrieved July 5, 2012, from <http://wiki.manchester.ac.uk/spheric>.
- SPHysics: Robert A. Dalrymple, Moncho Gómez-Gesteira, Ben Rogers, Alejandro Crespo, Muthukumar Narayanaswamy, Shan Zou, Andrea Panizzo, retrieved July 5, 2012, from <http://wiki.manchester.ac.uk/sphysics>
- Swegle J.W., Hicks D.L. and Attaway S.W., Smoothed particle hydrodynamics stability analysis, *J Comp. Phys.* 1995; **116(1)**:123-134.
- Tatard L., Planchon O., Wainwright J., Nord G., Favis-Mortlock D., Silvera N., Ribolzi O., Esteves M. and Huang, C., Measurement and modelling of high-resolution flow-velocity data under simulated rainfall on a low-slope sandy soil, *J. Hydrol.*

- 2008; **348(1-2)**:1–12.
- Toro E.F., *Shock Capturing Methods for Free Surface Shallow Water Flows*, Wiley: New York, 1999.
- Vacondio R., *Shallow Water and Navier-Stokes SPH-like numerical modelling of rapidly varying free-surface flows. Ph. D Thesis*, 2010.
- Vacondio R., Rogers B.D. and Stansby P.K., Accurate particle splitting for smoothed particle hydrodynamics in shallow water with shock capturing, *Int. J. Numer. Meth. Fluids* 2011; doi: 10.1002/flid.2646.
- Vacondio, R., Rogers, B.D., Stansby, P.K., Mignosa, P., SPH modeling of shallow flow with open boundaries for practical flood simulation, *J. Hydraul. Eng.* 2012a; **138(6)**: 530-541.
- Vacondio R., Rogers B.D. and Stansby P.K., Smoothed Particle Hydrodynamics: Approximated zero-consistent 2-D boundary conditions and still shallow-water tests, *Int. J. Numer. Meth. Fluids* 2012b; doi: 10.1002/flid.2559.
- Vasconcelos J.G and Marwell D.T.B., Innovative simulation of unsteady low-pressure flows in water mains, *J. Hydraul. Eng.* 2011; **137(11)**: 1490-1499.
- Vasconcelos J.G., Wright S.J. and Roe P.L., Current issues on modeling extreme inflows in stormwater systems, *J. Water Man. Model* 2006a; R225-19, doi: 10.14796/JWMM.R225-19.
- Vasconcelos J.G., Wright S.J. and Roe P.L., Improved simulation of flow regime transition in sewers: two-component pressure approach, *J. Hydraul. Eng.* 2006b; **132(6)**:553-562.
- Vasconcelos J.G. and Wright S.J., Comparison between the two-component pressure approach and current transient flow solvers, *J. Hydraul. Res.* 2007; **45(2)**:178-187.
- Vieux B.E. and Gauer, N., Finite-element modeling of storm water runoff using GRASS GIS, *Comput. Aided. Civ. Inf.* 1994; **9**:263-270.
- Vila J.P., On particle weighted methods and Smooth particle hydrodynamics, *Math. Models Methods Appl. Sci.* 1999; **9(2)**:161-209.
- Violeau D., *Fluid Mechanics and the SPH Method: Theory and Applications*. Oxford University Press, Oxford, 2012.
- Wang Z. and Shen H.T., Lagrangian simulation of one-dimensional dam-break flow, *J. Hydraul. Eng.*, 1999; **125**:1217-1220.
- Woolhiser D.A., Smith R.E. and Giraldez J.-V., Effects of spatial variability of saturated hydraulic conductivity on Hortonian overland flow, *Water Resour. Res.* 1996; **32(3)**:671-678.
- Zhang W.H. and Cundy T.W., Modeling of two-dimensional overland Flow, *Water Resour. Res.* 1989; **25(9)**:2019-2035.
- Zhu Y., Fox P.J. and Morris J.P., A pore-scale numerical model for flow through porous

media, *Int. J. Numer. Anal. Met.* 1999; **23**:881-904.

